Synergistic Artificial Interlayer to Enhance the Homogeneity of Zinc-ion Flux for Dendrite-free Zinc Metal Anodes

by

Jialiang Wang

A thesis submitted in partial fulfillment of the requirements for the degree of

Master of Science

Department of Mechanical Engineering
University of Alberta

Abstract

The decreasing availability of fossil fuels and increasing environmental concerns highlight the necessity to seek sustainable and environmentally friendly electrochemical energy sources for modern energy storage. Among potential candidates, aqueous Zn-ion batteries (AZIBs) are considered highly promising due to their safety, low cost, and eco-friendliness, especially compared to the safety hazards and economic challenges of popular lithium-ion batteries (LIBs). However, AZIBs face several challenges, including weak separator strength, inferior cathode performance, and the potential failure of the Zn anode due to issues like dendrite growth, passivation, and corrosion of pristine Zn in electrolytes. Among these challenges, metal anode failure is considered a significant factor in AZIB failure.

To overcome this issue, various methods have been explored to achieve a highly stable Zn metal anode, such as designing novel structures, interfacial engineering, and introducing electrolyte additives. A 3D conductive host, e.g., zeolitic imidazolate framework-8 (ZIF8), is often considered an effective strategy as it provides a porous framework with an enlarged effective specific surface area, which can reduce local current densities, suppress dendrite formation, and buffer volume expansion during Zn plating.

In Chapter 1, the demand for high-performance AZIBS and short terms of present zinc

anode will be described and discussed.

Chapter 2 is a literature review on artificial interlayers for functional AZIBS, background of AZIBS and functionality of interlayers will be discussed, how the dendrites and side reactions are suppressed, followed by a summary of some different interlayers from published articles. The reason for focusing on the anode coating layer is to decrease the contact area of electrolyte and anode to suppress the corrosion and dendrites formation as the Zn ions diffusion paths are not blocked even the coating layer can aid the transmission of Zn ions.

Chapter 3 will describe the methodologies and techniques used in my project, and their purpose and criteria will be illustrated as well.

Chapter 4 is a demonstration of ZIF8-supported g-C_3N_4(g-C_3N_4@ZIF8) as the coating layer in AZIB achieved a decent electrochemical performance and satisfying sustainability. g-C_3N_4 sustained by ZIF8 can modulate and adjust the Zn^{2+} flux, leading to a reduction in the corrosion area of the zinc anode in the water-based electrolyte. Additionally, with the low conductivity of g-C_3N_4 and ZIF8, Zn^{2+} can only migrate through the interlayer and deposit between the interlayer and Zn under the external electrical field. With this effective interlayer coating on the Zn anode, the symmetric cell can achieve 6,200 hours of cycling at 0.25 mA cm^{-2}/0.25 mAh cm^{-2} and 1,000 hours of cycling at 5 mA cm^{-2}/1 mAh cm^{-2}, with remarkable rate performance that can reach 40 mA cm^{-2}. When coupled with a flexible

V_2O_5 nanopaper cathode, the full cell exhibits the ability to achieve over 1,000 stable cycles at a rate of 1A g^{-1}. Hence, an artificial interlayer on the Zn anode can weaken corrosion and suppresses dendrite growth by evenly distributing ions and electrons, mitigating and slowing down the formation of the non-uniform anode surface. This design deaccelerates the growth speed and reduces the number of dendrites, enabling reversible Zn stripping/plating.

Chapter 5 briefly summarizes previous chapters about research progress and experiment results and these work's contribution to literature. It will also provide several suggestions for future work.

Preface

This thesis is an original work by Jialiang Wang under the supervision of Dr. Ge Li from the Department of Mechanical Engineering at the University of Alberta.

Chapter 4 is written based on an article that will be submitted to journal publications. This article cooperated with Ph.D. Xuzi Zhang, who's in charge of the DFT calculation part, as I finished the original manuscript, organized figures, and managed references of other parts. Dr. Ge Li contributed to the supervision, review and editing of the manuscript.

This thesis is dedicated to

my parents, Lei Wang and Shihong Liang,

my grandmother Xiulan Li,

for their love and health

Acknowledgements

List of Contents

List of Tables

List of Figures

List of Abbreviations

Chapter 2

AZIB	Aqueous zinc ion battery
AC	Active carbon
ZIB	Zinc ion battery
LIB	Lithium-ion battery
SHE	Standard hydrogen electrode
3D	Three-dimensional
HER	Hydrogen evolution reactions
PVDF	Polyvinylidene fluoride
PFSA	Perfluorosulfonic acid
NGO	Nitrogen (N)-doped graphene oxide
CNT	Carbon nanotube
GO	Graphene oxide
rGO	Reduced graphene oxide
Ppy	Polypyrrole
PANZ	Polyacrylonitrile
MOFs	Metal organic frameworks
BET	Brunauer Emmett Teller
SEM	Scanning electron microscope
KL	Kaolin
F-TiO$_2$	faceted-TiO$_2$
PANI	polyaniline
PMMA	polymethylmethacrylate

PVB   Polyvinyl butyral

Chapter 4

2-MIM   2-methylimidazole

XRD   X-ray Diffraction

TEM   Transmission electron microscope

DFT   Density functional theory

VASP   Vienna Ab initio Simulation Package

PBE   Perdew-Burke-Ernzerhof

GGA   Generalized gradient approximation

CV   Cyclic voltammetry

CA   Chronoamperograms

CE   Coulombic efficiency

2D   Two-dimensional

EIS   Electrochemical impedance spectroscopy

GCD   Galvanostatic charge/discharge

Chapter 1. Introduction

1.1 Motivation

Since the first electrochemical cell (the voltaic pile) was invented by Italian physicist Alessandro Giuseppe Antonio Anastasio Volta, zinc metal acted as the anode in the first batteries. The invention of the battery signaled a breakthrough in the ability of humans to harness electrical energy in a convenient manner, opening up an abundance of exciting applications until today. Nowadays, along with the technological development of the past 200 years, the capacity, stability, and portability of modern batteries are dramatically enhanced. The magnum opus of contemporary batteries is the lithium-ion battery (LIB). However, the explosive growth of demand for LIBs is restricted by the high cost of lithium-based raw material due to the low storage of lithium elements on earth, and the trade-off between energy density and safety is another brutal constraint of further application of LIBs.

Alternatively, aqueous zinc-ion batteries (AZIBs) stand out and are regarded as one of the most favorable substitutes for LIBs relying on the safety and cheapness of zinc metal. Firstly, the low redox potential of zinc (-0.76 V vs SHE [1]) offers enhanced stability in water-based electrolytes compared to lithium, as the redox potential of lithium is -3.04 V vs SHE [2]. Hence, the fabrication of AZIBs can be conducted under ambient atmospheric conditions, whereas lithium-ion batteries (LIBs) require an inert atmosphere. This distinction underscores the superior safety and economic viability of AZIBs fabrication [3,4]. Secondly, the abundance of zinc element is much higher than lithium means the raw material of AZIBs is much cheaper than LIBs [5]. Lastly, zinc has a high theoretical capacity (820 mAh g-1[1]/ 5854 mAh cm-3), which offers a significant advantage in terms of large-scale energy storage capabilities. Nevertheless, AZIBs still have several crucial obstacles that need to be overcome, including dendrite growth, passivation, and corrosion of

pristine Zn in the electrolytes [3], commonly considered significant factors in AZIBs failure.

1.2 Current Challenges for Zinc Metal Anode

(1) Dendrite growth in Li metal anodes [21]and Zn metal anodes [22] are both fatal factors that lead to internal short circuits caused by ions' inhomogeneous deposition. Especially Young's modulus of Zn is 108 GPa, which is one order of magnitude higher than Li (5 GPa) [23], indicating the Zn dendrites have better mechanical properties and are easier to penetrate the separator, resulting in poor cycling ability.

(2) Side reactions are challenges that require resolution. $ZnSO_4$ is a widely used weak acidic electrolyte in AZIBS [25,26], leading to strong hydrogen evolution reactions (HER); the hydrogen bubble can bulge the sealed cells [27] and may cause the explosion of the battery. Furthermore, the reduced concentration of H^+ ions can increase the pH environment of the electrolyte so that the zinc anode will react with the hydroxide ions and form a passivation layer which will deaccelerate the zinc ion diffusion rate and boost the internal impedance [25]. The side reaction formulas are displayed as follows [24]:

$$2H_2O + 2e^- \rightarrow H_2 + 2OH^-, \tag{1}$$

$$4Zn^{2+} + 6OH^- + SO_4^{2-} \rightarrow Zn_4SO_4(OH)_6, \tag{2}$$

$$Zn^{2+} + 2OH^- \rightarrow Zn(OH)_2 \tag{3}$$

$$Zn(OH)_2 \rightarrow ZnO + H_2O. \tag{4}$$

Nonetheless, side reactions are not solely ruining the performance of AZIB [28]. For instance, the formation of dendrites can expand the surface area of the zinc anode leading to stronger HER reactions [29], and stronger HER reactions will produce more $Zn_4SO_4(OH)_6$, $Zn(OH)_2$, and ZnO particles on the surface of electrode resulting in an uneven surface and electrode polarization becoming sever[30]. These factors can promote dendrite formation and ultimately lead to the catastrophic failure of AZIB.

2

Chapter 2. Literature Review

Anode Artificial Interlayers for Dendrite-Free Aqueous Zinc-ion Batteries

2.1   Abstract

Nowadays, with the rapidly growing demand for energy storage devices in electrical vehicles, mobile phones, wearable gadgets, *etc*. Aqueous zinc ion batteries (AZIBs) are regarded as one of the most hopeful candidates for future grid-scale energy storage owing to their high safety level, low cost, and environmentally friendly. However, dendrite formation and side reactions are severely hindering the stability and efficiency of AZIBs. To settle these problems, the zinc metal anode surface modification is an assuring method and strategy to regulate the reaction at the anode and electrolyte interface and mitigate the dendrite formation and corrosion. Thus, the surface coating should have good tolerance to surface change, high resistance to solve in aqueous electrolyte, good mechanical strength, and will not block the diffusion path of zinc ions to the anode surface. Moreover, surface modification has the characterization of easy synthesis and effectiveness. In this review, advanced artificial interlayers will be discussed and concluded in two groups, inorganic and polymer coating. In the end, a summary of all the details from these examples was provided, such as preparation methods, function structures, voltage hysteresis, and lifespan, along with a dedicated evaluation of the related challenges, constructive solutions, and prospects of functional AZIBs.

2.2 Background

The dendritic Zn is usually formed from unevenly distributed Zn^{2+} flux near the surface of the anode with random nucleation, which will further introduce the so-called "tip effect" [6-8]. Hence, the preferential deposition at the Zn-tip is the primary reason for zinc dendrites. Based on this point, extensive efforts have been devoted to achieving a highly stable Zn metal anode, such as designing a novel structure for the Zn anode[9], interfacial engineering [10], or introducing electrolyte additives [11]. 3D conductive host construction is usually considered an effective strategy due to the porous framework with an enlarged effective surface area which not only reduces local current densities and suppresses the large dendrites formation process but also buffers the volume expansion during Zn plating [12]. Nevertheless, as nucleation sites increase, hydrogen evolution and corrosion reactions are also more likely to happen [13]. Electrolyte additives have been widely reported as effective methods to regulate Zn^{2+} flux or reduce the active molecules in solvated ions. However, the additional extra cost of these additives is a potential disadvantage [3]. In comparison, a functional interlayer that is inertia and allows for even Zn^{2+} penetrability can not only regulate the Zn^{2+} flux but also inhibit side reactions between the electrolyte and Zn electrode. As a result, the construction of the functional interlayer is one of the most effective and promising methods.

Anode artificial interlayer possesses the following advantages (1) Easy to synthesize and cheap materials. (2) Reduce the contact area of the electrolyte and zinc anode to inhibit the side reaction on the zinc anode. (3) Regulate the zinc ion migration by the intrinsic characteristics of the material. There have been several materials reported functional in AZIBs, such as TiO_2[17], PFSA [18], NGO [19], Kaolin [20], etc. All the above-mentioned materials will be discussed in the following review with a detailed analysis of mechanisms, synthesis, and results. The artificial interlayer will be categorized into two groups, inorganic and polymer coating, based on their characteristics.

Table 1. A survey of modified Zn anodes and corresponding electrochemical properties in Zn‖Zn symmetric cells.

Sample	Symmetric cells			
	Current density (mA cm^{-2}), capacity density (mAh cm^{-2})	Voltage hysteresis	Cycle life	Reference
Zn/C$_3$N$_4$@ZIF-8	0.25, 0.25	110mV	6000h	My work
	5, 1	115mV	1000h	My work
	10, 1	150mV	250h	My work
Carbon-based materials				
Zn/C$_3$N$_4$	2,2	~80mV	500h	[32]
	10,5	~200mV	120h	
Zn/NGO	1,1	34mV	1200h	[37]
	5,5	96mV	300h	
Zn/CNT	0.15, 0.5	120mV	600h	[33]
Zn/carbon nanofiber	0.5,0.5	~50mV	800h	[34]
	5,1	~100mV	1200h	
Zn/GO	Not provided			[35]
Zn/rGO	0.2,0.2	~30mV	2000h	[36]
	0.4,0.4	~35mV	2000h	

	1,1	~40mV	1200h	
Metal oxides and inorganic acid salts				
Zn/nano-CaCO$_3$	0.25,0.05	105mV	836h	[41]
Zn/Kaolin	4.4,1.1	~140mV	800h	[42]
Zn/Al$_2$O$_3$	1,1	36.5mV	500h	[62]
Zn/ZnF$_2$	0.5,0.5	80.5mV	720h	[44]
Zn/ZnO/C	0.25,0.25	56mV	2000h	[15]
	2,1	~80mV	500h	
	5,1	~150mV	700h	
	10,2.5	~200mV	240h	
Zn/TiO$_2$	1,1	40.9mV	150h	[40]
Zn/Sc$_2$O$_3$	1,1	71mV	200h	[48]
	0.5,0.5	~55mV	300h	
	2,2	~40 mV	250h	
Metals and alloys				
Zn/Cu	1,0.5	~60mV	1500h	[45]
Zn/Sn	1,1	28mV	800h	[49]
Zn/Ga-In alloy	0.25,0.25	~48mV	2100h	[46]
	1,0.1	~90mV	1200h	

	5,0.1	~224mV	360h	
Zn/Ag	0.2,0.2	38mV	1450h	[47]
	1,1	46mV	350h	
	2,2	52mV	150h	
Zn/In	0.2,0.2	54mV	1500h	[48]
	1,1	~200mV	520h	
Zn/P	2,0.5	25mV	3300h	[66]
	5,1.25	33mV	3200h	
	10,2.5	53mV	1900h	
	20,30	102.4mV	300h	
	15,48	210mV	100h	
Polymer materials				
Zn/Ppy	2,1	45mV	540h	[68]
Zn/ β-PVDF	0.25,0.05	80mV	2000h	[52]
	1.6,0.3	100mV	100h	
Zn/PANZ	1,1	75mV	1145h	[60]
Zn/Polyacrylonitrile	1,1	75mV	1145h	[49]
Zn/PFSA	1,0.5	~80mV	1500h	[50]
	1,1	~90mV	800h	

Zn/502 glue	0.5,0.25	100mV	800h	[69]
	2,1	110mV	400h	
	4,2	120mV	350h	
Zn/PVB	0.5,0.5	~210mV	2200h	[67]
Metal organic frameworks (MOFs)				
Zn/ZIF-8	2,1	~52mV	1250h	[56-58]
	2,2	~52mV	700h	

Table 2.A survey of modified Zn anodes and corresponding electrochemical properties in Zn||Cathode Full cells.

	Full cells			
Sample	Current density, Cathode	Voltage retention	Cycle life (cycles)	Reference
Carbon-based materials				
Zn/C$_3$N$_4$	1 A g^{-1}, AC	94.1%	500	[32]
	1 A g^{-1}, MnO$_2$	97.1%	1000	
Zn/NGO	0.5C, LMO(LiMn$_2$O$_4$)	94%	180	[37]
Zn/CNT	5 mA cm^{-2}, CNTs@MnO$_2$	100%	11000	[33]
Zn/carbon nanofiber	1 A g^{-1}, MnO$_2$	108.3%	420	[34]
Zn/rGO	1 A g^{-1}, AC	88.5%	5000	[36]
Zn/graphite	5 A g^{-1}, V$_2$O$_5$	84%	1500	[38]
Metal oxides and inorganic acid salts				
Zn/nano-CaCO$_3$	1 A g^{-1}, MnO$_2$	86%	1000	[41]
Zn/Kaolin	0.5 A g^{-1}, MnO$_2$	100%	600	[42]
Zn/Al$_2$O$_3$	1 A cm^{-2}, MnO$_2$	89.4%	1000	[62]
Zn/ZnF$_2$	0.6 A cm^{-2}, MnO$_2$	89%	3000	[44]

Zn/ZnO/C	1 A g^{-1}, MnO$_2$	75%	1000	[15]
	1 A g^{-1}, V$_2$O$_5$	N/A	800	
Zn/TiO$_2$	1 A g^{-1}, MnO$_2$	85%	1000	[40]
Zn/Sc$_2$O$_3$	10 A g^{-1}, MnO$_2$	82.4%	1000	[118]
Metals and alloys				
Zn/Cu	10 C, MnO$_2$	94.2%	500	[45]
Zn/Sn	1 A g^{-1}, MnO$_2$	83.1%	900	[49]
Zn/Ga-In alloy	1 A g^{-1}, MnO$_2$	50%	1000	[46]
Zn/Ag	5 A g^{-1}, V$_2$O$_5$	60%	1500	[47]
Zn/In	1 A g^{-1}, AC	100%	5000	[48]
Zn/P	1 A g^{-1}, MnO$_2$	77.2%	1000	[66]
Polymer materials				
Zn/Ppy	5 A g^{-1}, MnO$_2$	96%	12000	[68]
Zn/ β-PVDF	1 A g^{-1}, V$_2$O$_5$	30%	4000	[52]
Zn/PANZ	0.5 A g^{-1}, MnVO(Mn-doped V$_2$O$_5$)	52%	1000	[60]
Zn/PFSA	0.5C, MnO$_2$	80%	500	[119]
Zn/502 glue	1 A g^{-1}, V$_2$O$_5$	59.3%	550	[69]
Zn/PVB	5C, MnO$_2$	86.6%	1500	[67]

Metal organic frameworks (MOFs)				
Zn/ZIF-8	0.5 A g^{-1}, MnO_2	76%	250	[56]

2.3 Inorganic Coating Layers for Aqueous Zinc-ion Batteries

Commonly inorganic coating layers can be divided into Carbon-based materials, alloys, metal oxides, acid salt, and organic based on their composites. From **Table 1** and **Table 2**, some researchers reported materials are summarized.

2.3.1 Carbon-based Materials

Carbon black [31], graphitic carbon nitride (g-C_3N_4) [32], carbon nanotube (CNT) [33], carbon nanofiber [34], graphene oxide [35], reduced graphene oxide (rGO) [36], nitrogen (N)-doped graphene oxide (NGO) [37] and graphite [38] are most used carbon-based materials as coating layers.

The main advantages of carbon-based materials are high conductivity, high stability, and large surface area; these characteristics can be found in some or all carbon-based materials. For example, Liang et al. [34] synthesized an N, O co-doped carbon nanofiber interlayer on a Zn metal anode surface. This sample had a porous surface of 7.07 m^2/g tested by Brunauer-Emmett-Teller (BET) surface area analysis (**Figure 1. a-b**). This trait can be used to lower the local current density, making the nuclei of zinc smaller and making the electric contribution more uniform [39]. SEM images of cycled zinc anode with carbon nanofiber are shown in **Figure 1. c**. The zinc metal anode with the carbon nanofiber clearly had a smooth surface, and the separator didn't entangle with the anode. Additionally, in (**Figure 1. d-g**), the symmetrical cell test of the carbon fiber-covered zinc anode showed lower nucleation overpotential under high current density (59.5mV under 5 mA cm^{-2}) and low current density (18.6 mV under 0.5 mA cm^{-2}). Also, a much longer life span compared with pure zinc anode achieved 1200 h cycling life under 5 mA cm^{-2}, 1 mAh cm^{-2} parameter. Also, in the full battery test, the carbon fiber-covered zinc anode versus MnO_2 battery sustained 400 h and with a 108.3% capacity retention after the cycling, as the pure zinc anode capacity decayed so fast that after 100 cycles, the capacity had dropped to around 25%.
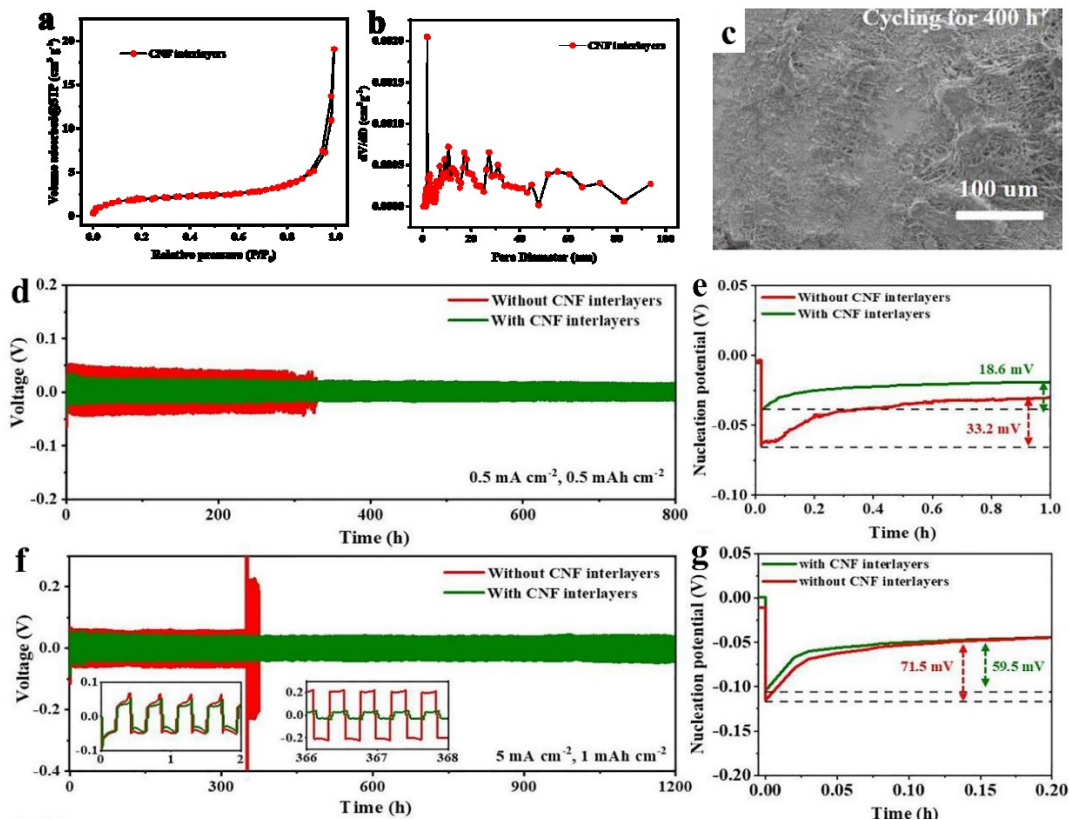
Figure 1. (a) N_2 adsorption/desorption isotherms and (b) corresponding pore size distribution of the CNF interlayers (c)The morphology of cycled Zn anode at the condition of 5 mA cm^{-2} and 1 mAh cm^{-2}. Cycling performance of Zn symmetric cells and corresponding nucleation overpotential under the parameter of (d, e) 0.5 mA cm^{-2} and 0.5 mAh cm^{-2}, and (f, g) 5 mA cm^{-2} and 1 mAh cm^{-2}. Copyright 2021, Elsevier

In addition, CNT is a popular interlayer material as well, Li et al. [33] applied CNT as the anode coating layer and at the same time used polyester-CNTs@MnO$_2$ as the cathode. In **Figure 2. a-b,** the CNT-covered zinc anode had lower overpotential in initial cycles and a much longer life span in the symmetric test which is 33 times longer than pure zinc symmetric cells (**Figure 2. d**). This led to a dramatically stable Mn^{2+}/Zn^{2+} hybrid full battery cycling time of 11000 cycles under 5 mA cm^{-2} (**Figure 2. e**). The large surface area and high conductivity of CNT are the main reasons for the improved electrochemical performance.

13
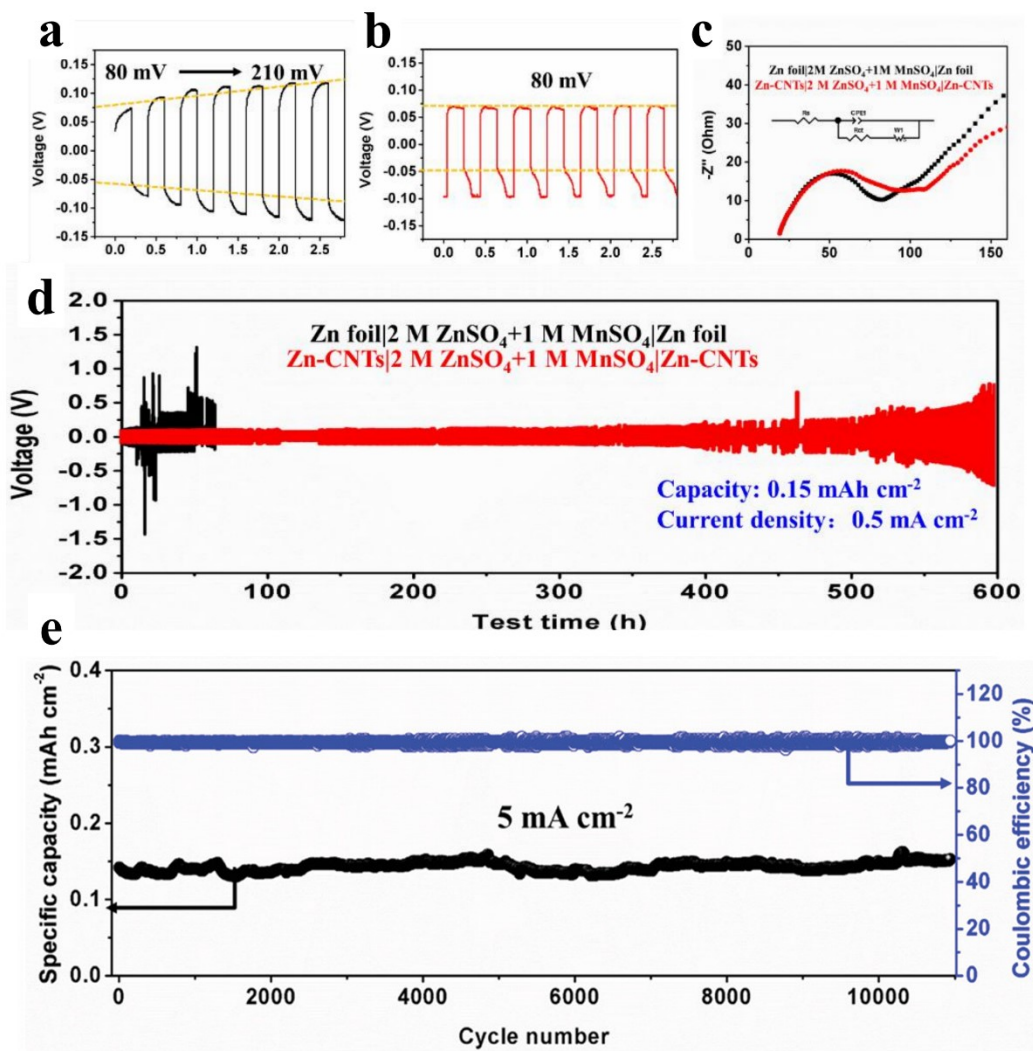
Figure 2. Capacity density in each cycle is 0.15 mAh cm^{-2}. The initial cycles of (a) used bare Zn foil or (b) Zn-CNTs symmetrical cells. (c) The EIS spectra of bare Zn and Zn-CNTs symmetric cells. (d) Symmetric cells with bare (black) and CNTs-Zn (red) at a current density of 0.5 mA cm^{-2} (e) the cycling performance of Mn^{2+}/Zn^{2+} hybrid full battery under 5 mA cm^{-2}. Copyright 2019, Wiley

Compared with the complexity of another anode synthesis, Zeng et al. [38] coated graphite on the zinc surface by simply pencil drawing. As depicted in **Figure 3. a,** the presence of the graphite coating layer impedes the formation of passivated byproducts and significantly mitigates dendrite

14

growth, **Figure 3. b** demonstrates that the graphite covered zinc anode had much lower nucleai overpotential (9 mV compared with 69 mV of pure zinc). Furthermore, the full cell test (**Figure 3. c**) was performed on a Zn–G anode versus $V_2O_5 \cdot x H_2O$ cathode; this device can output a power density of 160 mAh g^{-1} at a current density of 5 A g^{-1} with a capacity retention of ≈84% over 1500 cycles.
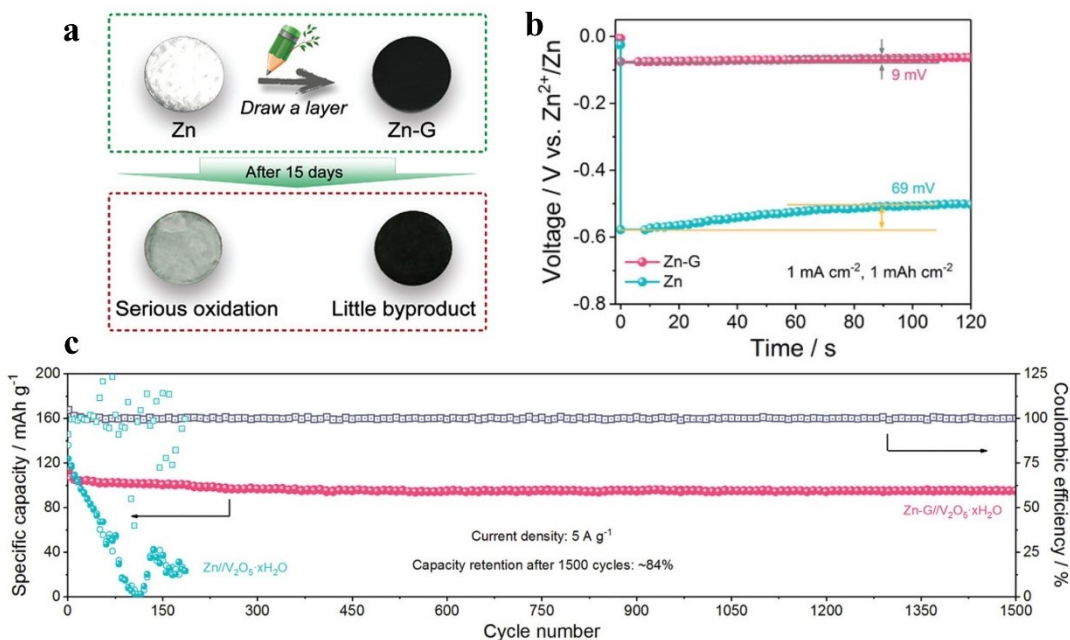
Figure 3. (a) Mechanism of pencil drawing graphite demonstration. (b) Nucleation overpotential of pure zinc and graphite-covered zinc anode symmetric cell test(c) Long-term cycling performance of Zn//$V_2O_5 \cdot xH_2O$ with Zn and Zn–G anodes at 5 A g^{-1} together with corresponding CEs. Copyright 2021, Wiley
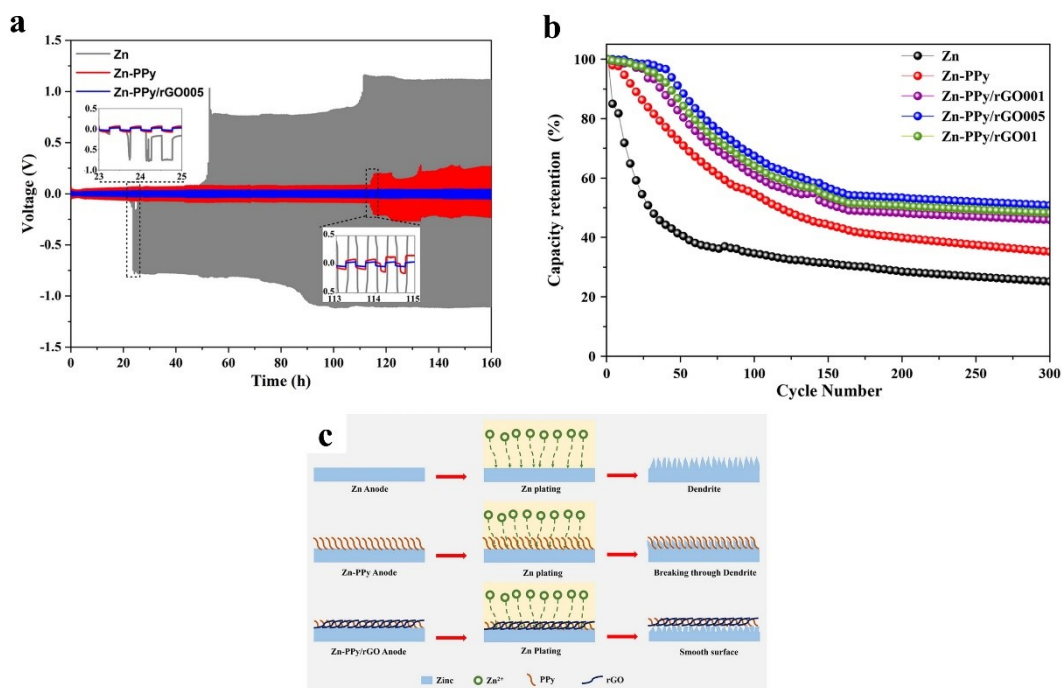
Figure 4. (a) Symmetric cell voltage profile under 0.5mA cm^{-2} (b) Capacity retention of the different samples (c) Mechanism of Ppy/rGO demonstration. Open Access 2022, Nature

Additionally, the wide range of morphological and property variations found in carbon-based materials provides a more adaptable framework for engineering coating layers. Sonti Khamsanga's group [64] reported that polypyrrole/reduced graphene oxide (PPy/rGO) can be used as the coating layer material. The high conductivity of PPy and rGO, and the excellent wetting ability of PPy guaranteed the sample covered zinc anode can keep good electrochemical performance and uniform zinc diffusion. In **Figure 4. a**, the symmetric cell of Zn- PPy/rGO sustained 160h at a current density of 0.5 mA/cm^2 and in the full cell test (**Figure 4. b**), the capacity retention of the Zn-PPy/rGO005 anode was 50% whereas the pure zinc anode only maintained a capacity retention of 25% after the 300th cycles. In addition, nitrogen doping is another popular technique due to the high zinc affinity of nitrogen doped groups. Jiahui Zhou's group reported [37] that (N)-doped graphene oxide (NGO) can direct the deposition of Zn in the 002 planes because the parallel

16

graphene layer can regulate the zinc ions diffusion and beneficial zincophilic-traits of the N-doped groups can aid the zinc ions go through the protecting surface. The NGO@Zn//NGO@Zn symmetric cell (**Figure 5. a**) demonstrated a 1200 h life cycle at a current density of 1 mA cm^{-2}. At a high current density of 5 mA cm^{-2} and capacity density of 5 mAh cm^{-2}(**Figure 5. b**), the cell stably sustained 300 hours with only 48 mV overpotential. In **Figure 5. c**, showing that the full cells assembled by his NGO@Zn anode and LiMn$_2$O$_4$ cathode maintained a high energy density of 164 Wh kg^{-1} after 178 cycles with a retention of over 80 percent.
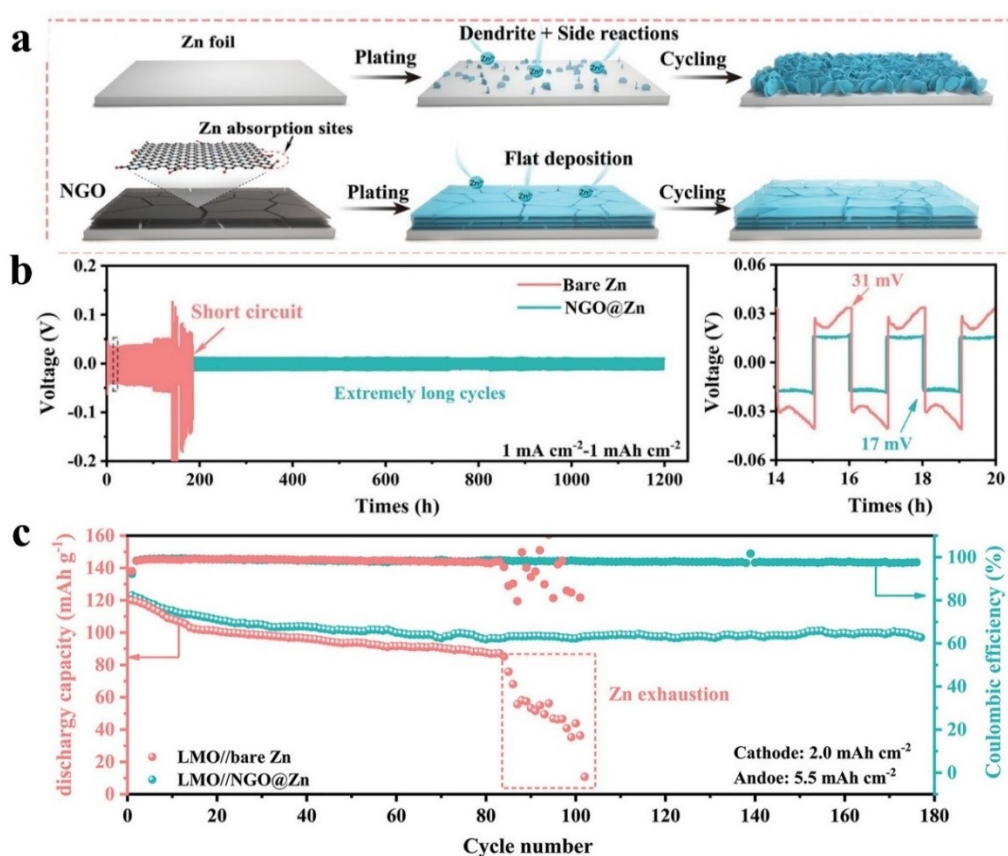
Figure 5. (a) Mechanism of NGO sheet demonstration. (b) Cycling performance of Zn symmetric cells and corresponding overpotential under the parameter of 1 mA cm^{-2} and 1 mAh cm^{-2} (c) The long-term performance of LMO//NGO@Zn and LMO//bare Zn cells with the LMO loading of 2.0 mAh cm^{-2} and an initial Zn foil thickness of 10 μm (5.5 mAh cm^{-2}) at 1 C (1 C = 148 mAh g^{-1}). Copyright 2021, Wiley

Furthermore, g-C$_3$N$_4$ as a semi-conductor with porous structure and robust zincophilicity due to nitrogen element richness in g-C$_3$N$_4$ was investigated as a functional interlayer by Liu et al [65]. The mechanism is demonstrated in **Figure 6. a**. G-C$_3$N$_4$ layer can block the contact between zinc anode and electrolyte also facilitate zinc ions diffusion. From **Figure 6. b**, the symmetric cell tests of Zn/g-C$_3$N$_4$ maintained stable much longer than pure zinc anode under 2 mA/cm^2, 2 mAh/cm^2 electrical parameters. The full cell test was performed with zinc anode versus MnO$_2$, demonstrated in **Figure 6. c**. The 3D-printed g-C$_3$N$_4$ coated zinc anode full cell exhibited excellent stability for 500 cycles with 94.1% at 1 A g^{-1}.
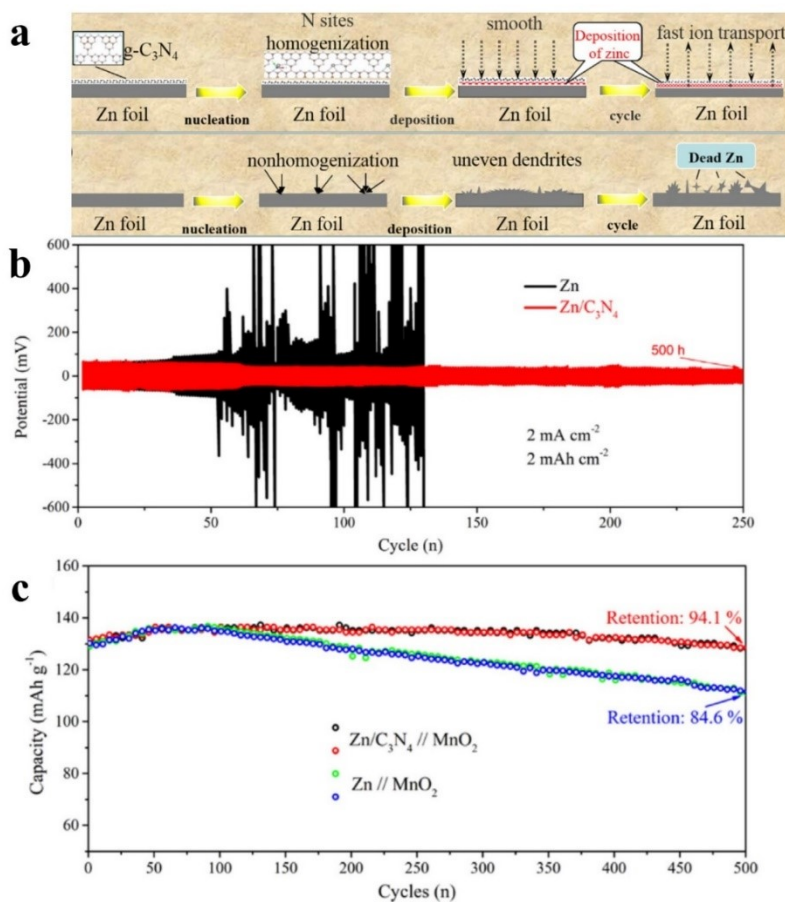
Figure 6. (a) Mechanism of g-C$_3$N$_4$ layer. (b) Cycling performance of Zn symmetric cells under the parameter of 2 mA cm^{-2} and 2 mAh cm^{-2} (c) The long-term performance of Zn//MnO$_2$ and Zn/C$_3$N$_4$//MnO$_2$ cells. Copyright 2021, Elsevier

2.3.2 Metal Oxides and Inorganic Acid Salts

To avoid the formation of zinc dendrites, rigid with high mechanical strength but porous that can't block the migration of zinc ion coating layers are desired. Many researchers reported that the metal oxides, including ZnO [15], TiO_2 [40] *etc*., and inorganic acid salts, including $CaCO_3$[41], Kaolin [42] *etc*., can fulfill the request.

Deng et al. [15] coated the ZnO/C hybrid layer on the surface of the zinc metal anode. From the SEM graphs (**Figure 7. f-g**), the ZnO/C hybrid layer undeniably inhibited the dendrite growth and side reaction. **Figure 7. h** is the mechanism schematic showing that the ZnO/C hybrid layer restricted the direct contact between the electrode and electrolyte, also **Figure 7. a** demonstrated the better hydrophilicity of the ZnO/C hybrid layer, which indicates better dendrite suppressing ability [43]. **Figure 7. a** shows that the ZnO/C hybrid layer coated had an excellent performance and ultralong cycle life of up to 2000h at 0.25 mA cm^{-2}, 0.25 mAh cm^{-2} with a lower voltage polarization (68mV) compared to pure zinc (134mV). The ZnO/C hybrid layer coated zinc anode versus MnO_2 full batteries also showed excellent stability and reliability (**Figure 7. b**). Li et al. [61] used porous rutile nano-TiO_2 as a coating layer. This layer had a uniform porous structure and good hydrophilicity, which successfully hindered the dendrite formation on the surface of the zinc anode. Additionally, Kangming Zhao's group stated the coating utility of TiO_2 as well [40]. By the literature, the corrosion process of a zinc plate is substantially inhibited, resulting in a decrease in the formation of gas and byproducts such as $Zn(OH)_2$. With the reduction in gas production on the zinc plate's outer surface, the interface between the electrolyte and anode remains effective, leading to an enhancement in the coulombic efficiency. Al_2O_3 was investigated by Huibing He's group as protecting layer[62]. Applying an ultrathin Al_2O_3 layer to the surface of a zinc plate enhanced the wettability of the zinc material and inhibited corrosion. This process effectively reduced the formation of Zn dendrites, which led to a substantial increase in the lifetime of Zn-Zn symmetric cells. Moreover, Zhang et al. [40] coated a faceted-TiO_2 (F-TiO_2) layer on the zinc anode surface

to investigate the role of crystal orientation of protective layers, revealing that 001 and 101 orientations of TiO_2 (F-TiO_2) can efficiently restrain dendrite growth. The symmetric cell test showed that the F-TiO_2 covered Zn anode had better durability (460 h at 1 mA cm^{-2} for 1 mAh cm^{-2}).
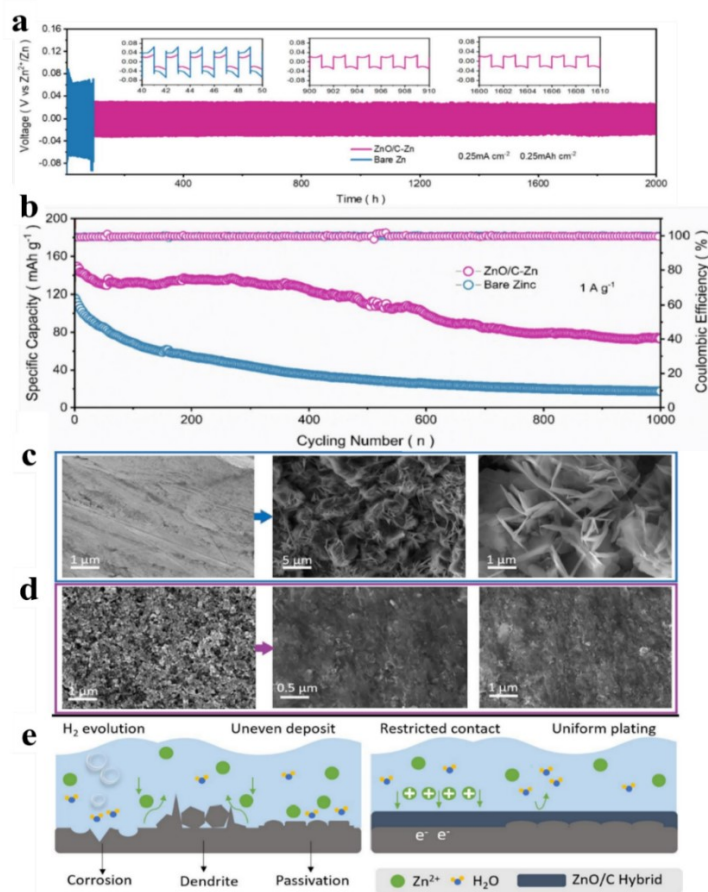
Figure 7. (a)Long-term symmetrical cell cycling using bare and coated Zn at 0.25 mA cm^{-2}, 0.25 mAh cm^{-2}.(b) Galvanostatic cycling of ZnO/C-Zn//MnO$_2$ batteries at 1 A g^{-1}. SEM image of (c) pristine Zn and (d) coated Zn after cycling. (e) Zn plating behavior on ZnO/C coated Zn and bare Zn. Copyright 2022, Elsevier
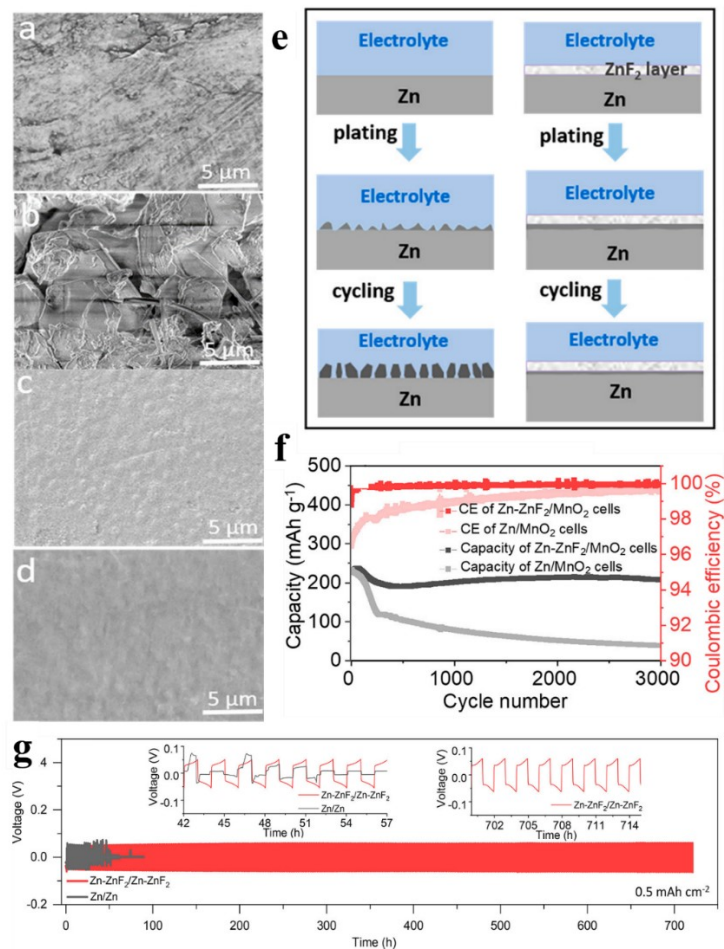
Figure 8. SEM images (a) (top view) of the bare Zn foil and (b) after plating/stripping for 100 cycles. (c) (top view) of the pristine Zn-ZnF$_2$ and (d) after plating/stripping measurements for 100 cycles. (e) Schematic depiction of the plating/stripping on bare Zn and Zn-ZnF$_2$. (f) The cycling performance of Zn//MnO$_2$ cells and Zn-ZnF$_2$//MnO$_2$ cells at a current density of 600 mA g^{-1}. Copyright 2021, American Chemical Society

21
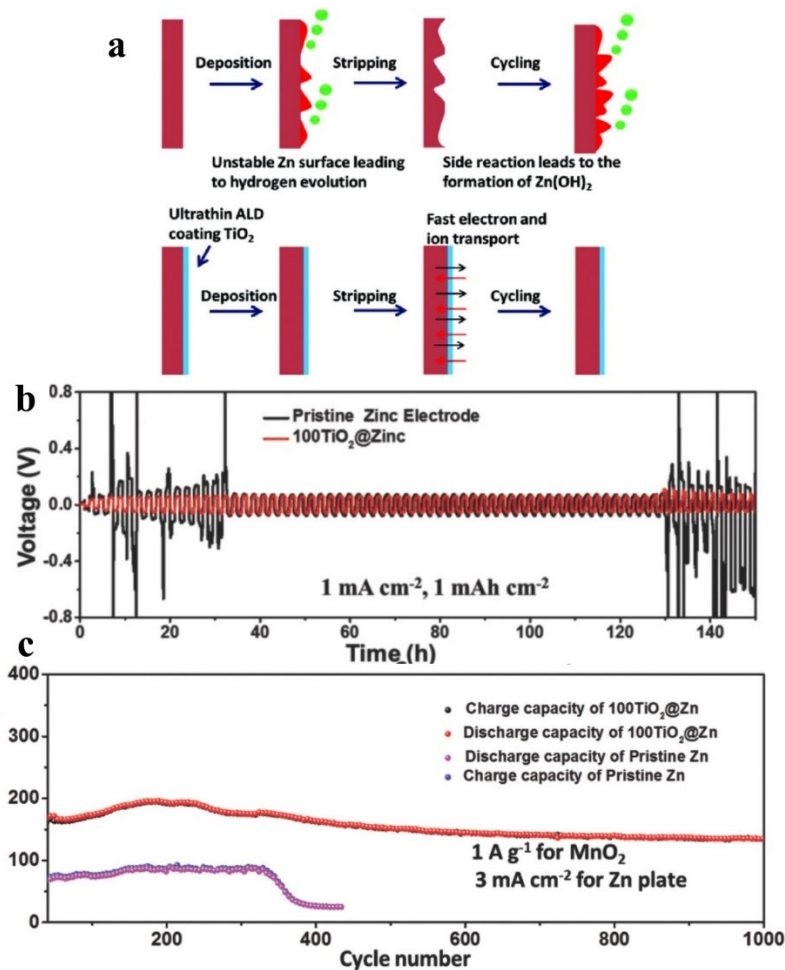
Figure 9. (a) Mechanism of TiO$_2$ layer. (b) Cycling performance of Zn symmetric cells under the parameter of 1 mA cm^{-2} and 1 mAh cm^{-2} (c) The long-term performance of TiO$_2$@Zn//MnO$_2$ and Zn//MnO$_2$ cells. Copyright 2018, Wiley

Inorganic acid salt ZnF$_2$ as a coating material for zinc anode was reported by Han et al. [44]. The ZnF$_2$ mechanism is shown in **Figure 8. a**, ZnF$_2$ is an insulator, but the crystal structure of ZnF$_2$ can provide low barrier diffusion channels for zinc ions. Therefore, the zinc ions deposited beneath the ZnF$_2$ layer form a smooth surface and prevent dendrite growth. The SEM images in **Figure 8. b-e** proved the mechanism again. From the figures, we can see that after the same cycles, large dendrites formed on the surface of the pure zinc anode, but Zn-ZnF$_2$ maintained a smooth surface.

22

The symmetric cell based on ZnF_2 covered zinc metal anode maintained around 120mV voltage hysteresis for over 700 h (**Figure 8. f**). When the Zn-ZnF_2 paired with a MnO_2 cathode, it sustained 3000 cycles with 85% retention (**Figure 8. g**) at a current density of 0.6 A g^{-1}. Kang et al. [41] discussed the ability of a nano-$CaCO_3$ coating to direct the stripping and plating of zinc at the interfaces between the nano-$CaCO_3$ layer and the zinc foil by its porosity. **Figure 9. a** demonstrated the mechanism of nano-$CaCO_3$, in the symmetric cell test (**Figure 9. b**) nano-$CaCO_3$ covered anode sustained longer than pure zinc under the same condition also in and Zn|$ZnSO_4$+$MnSO_4$|CNT/MnO_2 full cell test **Figure 9. c** the battery with a nano-$CaCO_3$-coated Zn anode delivers a higher discharge capacity of 177 at 1 A g^{-1} after 1000 cycles compared with the bare zinc anode. Deng et al. [42] declared that Kaolin is a possible functioning coating layer of AZIBs. Kaolin has a general formula of $Al_2Si_2O_5(OH)_4$, which has a layered silicate structure [63]. **Figure 10. a** is the mechanism schematic of the Kaolin coating layer, **Figure 10. b** shows the symmetric cell test result of KL-Zn (Kaolin covered Zinc anode) at 4.4 mA cm^{-2}, 1.1 mAh cm^{-2} sustained 800h and the result of full cell test **Figure 10. c** verified that the Kaolin coating layer can protect the zinc anode and improve the electrical performance.
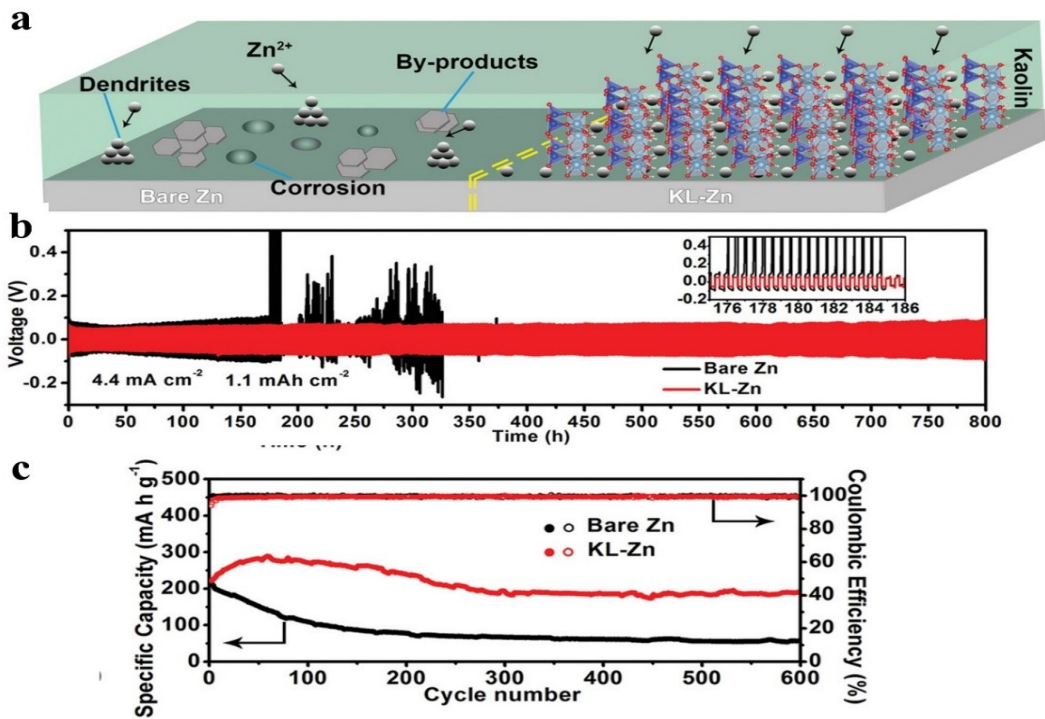
Figure 10. (a) Mechanism of Kaolin layer. (b) Cycling performance of Zn symmetric cells under the parameter of 4.4 mA cm^{-2} and 1.1 mAh cm^{-2} (c) The long-term performance of Zn//MnO$_2$ and KL-Zn//MnO$_2$ cells under current density 0.2 A g^{-1}. Copyright 2019, Wiley

In these studies, selected metal oxide and inorganic acid salts aided the sustainability and stability of batteries and successfully suppressed dendrite formation and side reactions relying on their inert chemical activity and porous structures. However, the weights of the inert layer would reduce the energy density of AZIBS, which is a significant drawback of Metal oxides and inorganic acid salts interlayer.

2.3.3 Metals and Alloys

Many kinds of metal were studied by researchers. Some are used as coating layers. For example, Cu [45], gallium–indium alloy [46], *etc.,* or used as hetero seeds, for instance, Ag [47], In [48], Sn [49], *etc.,* both utilities can be helpful to achieve dendrite-free zinc anode.
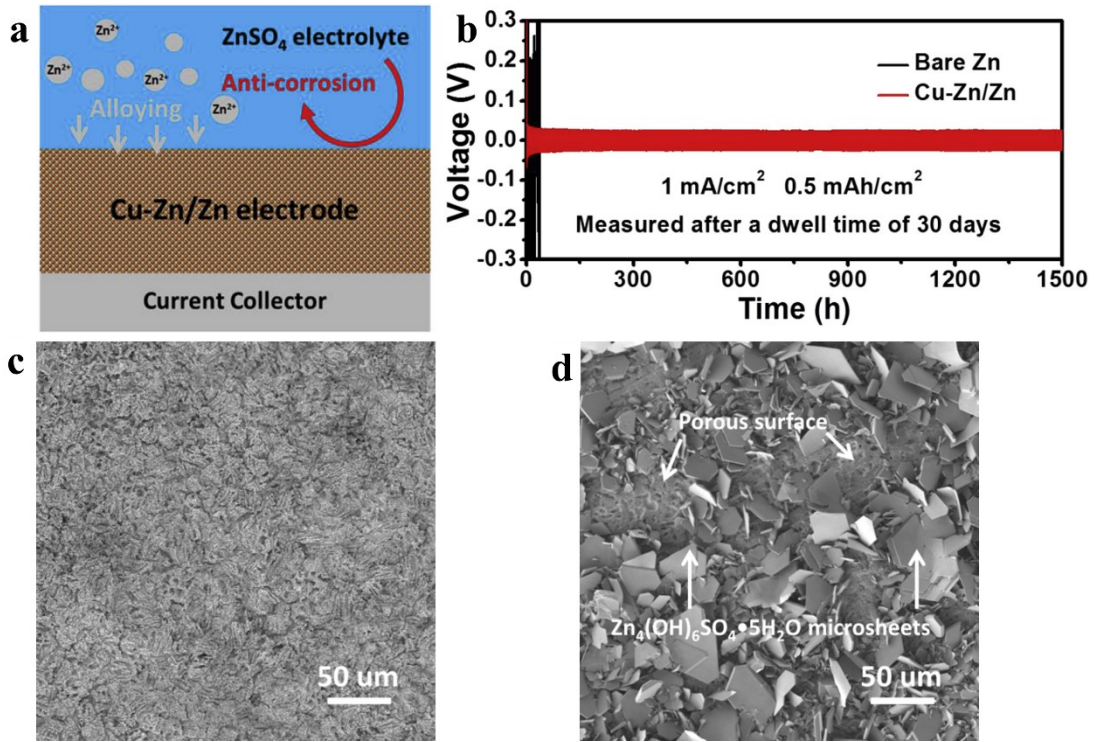
Figure 11. (a) Schematic depiction of the plating/stripping on bare Zn and Zn-Cu. (b) Voltage profiles of Cu/Zn-30d‖Cu/Zn-30d symmetric cell at 1 mA/cm^2 and 0.5 mAh/cm^2. Top-view SEM image of the (c)Cu/Zn electrode and (d) the bare Zn electrode after 100 stripping/plating cycles at 1 mA/cm^2 and 0.5 mAh/cm^2. Copyright 2020, Elsevier

Cai's group [45] coated Cu on the surface of zinc by replacement reaction and then annealed the sample to form Zn/Cu integrated structure. As **Figure 11. (a)**, showing that the mechanism of the Cu interlayer is acting as a protecting layer to avoid direct contact of electrolyte and electrode so that can eliminate the zinc side reactions. Moreover, Cu has high conductivity and can form zinc copper alloy to guide the deposition of Zn ions [50]. **Figure 11. (b)** demonstrates that even after 30 days of electrolyte immersion, the symmetric cell based on Cu/Zn‖Cu/Zn sustained for 1500h with ~46 mV overpotential under 1 mA cm^{-2}, 0.5 mAh cm^{-2} parameters. Lu et al. [47] introduced Ag as depositing seed of zinc leads to uniform deposition, and the SEM images of cycled anode

surface were provided, as shown in **Figure 12. (d)**. Consequently, the Zn anode coated with Ag demonstrates remarkable performance, allowing for sustained plating and stripping cycles lasting up to 1450 hours. This is achieved at a low overpotential in symmetric cells under a current density of 0.2 mA cm^{-2} (**Figure 12. (b)**), while full cells paired with a V_2O_5-based cathode sustained over 1500 cycles with a 180 mAh g^{-1}, which is better than the bare zinc anode full cell (**Figure 12. (c)**).
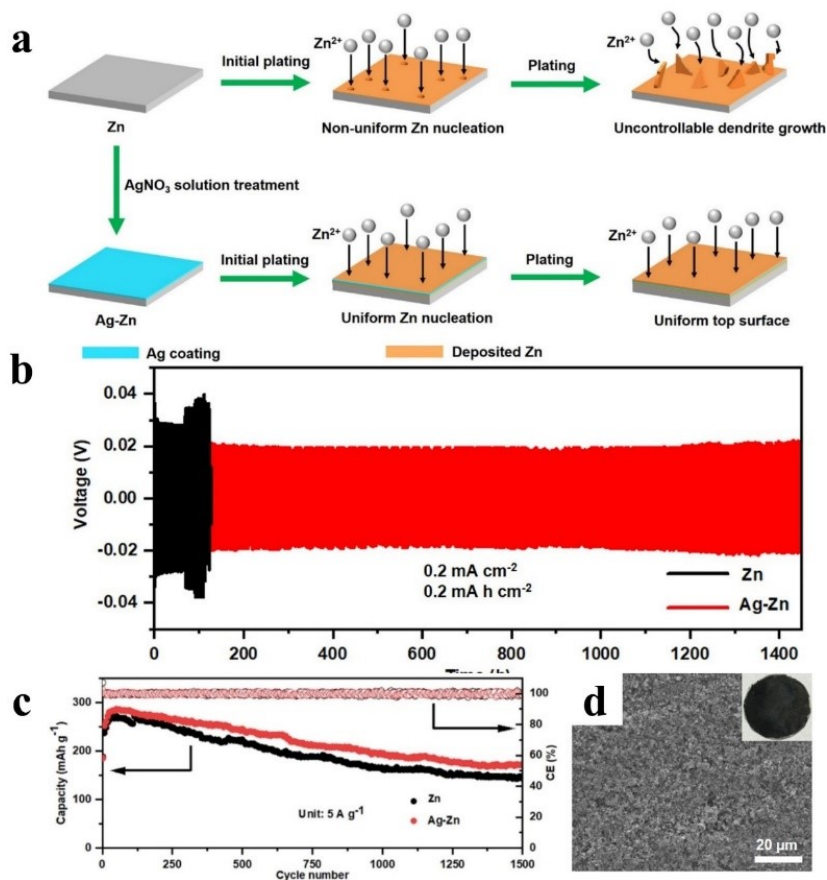
Figure 12. (a) Mechanism of Ag-Zn layer. (b) Cycling performance of Zn symmetric cells under the parameter of 0.2 mA cm^{-2} and 0.2 mAh cm^{-2} (c) The long-term performance of Zn//MnO$_2$ and Ag-Zn//MnO$_2$ cells under current density 5 A g^{-1}. (d) SEM images and optical images (insets) of Ag-Zn foil. Copyright 2021, American Chemical Society
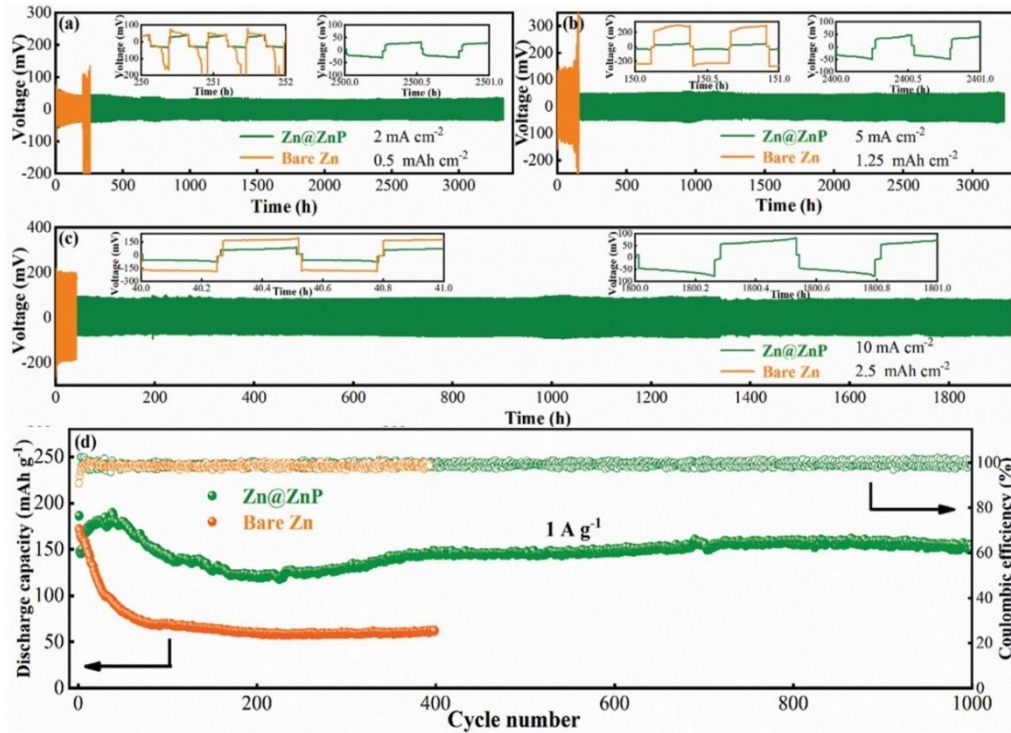
Figure 13. Symmetric cells cycled at multiple current densities and areal capacities of 2 mA cm^{-2}, 0.5 mAh cm^{-2} (a); 5 mA cm^{-2}, 1.25 mAh cm^{-2} (b); 10 mA cm^{-2}, 2.5 mAh cm^{-2} (c) and 15 mA cm^{-2}, 48 mAh cm^{-2}. (d)Zn/MnO2 full cells at 1 A g^{-1}. Copyright 2021, Wiley

Cao et al. [66] applied phosphorus (P) atoms to aid ion transfer and reduce the electrochemical activation energy of zinc ions plating and stripping. Besides, the P atoms can lower the energy barrier in Zn^{2+} transferring. The results showed that the Zn@ZnP anode in the symmetric cell can be stably cycled at multiple different current densities and areal capacities of 2 mA cm^{-2}, 0.5 mAh cm^{-2} (**Figure 13. (a))**; 5 mA cm^{-2}, 1.25 mAh cm^{-2}(**Figure 13. (b))**; 10 mA cm^{-2}, 2.5 mAh cm^{-2} (**Figure 13. (c))** and 15 mA cm^{-2}, 48 mAh cm^{-2}. Notably, the Zn/MnO$_2$ full cell can attain 1000 cycles with a discharge capacity of 154.4 mAh g^{-1} at 1 A g^{-1}(**Figure 13. (d))**.

The results obtained above proved the metal and alloy interface could reduce side reactions and inhibit dendrite growth, but some precious metals were used, which will increase the cost of AZIB. That is why we are searching for a substitute for lithium-ion batteries.

27

2.4 Organic Coating Layers for Aqueous Zinc-ion Batteries

2.4.1 Polymer Materials

The polymer materials comprise polyaniline (PANI), polypyrrole (Ppy) [68], polymethylmethacrylate (PMMA) [51], β-phase poly(vinylidene difluoride) (β-PVDF) [52], Polyacrylonitrile (PANZ) [53], polyvinyl butyral (PVB) [67], cyanoacrylate adhesive(502 glue) [69] etc. The attractive properties of polymers materials are adequate hydrogen bonding and loads of functional groups [54-55].

Chen et al. [60] reported that the PAN solution containing zinc trifluoromethanesulfonate (Zn(OTF)$_2$) on zinc foil (PANZ@Zn) could reduce the resistance of Zn anode and the cyano groups (-CN) can facilitate the transportation of zinc ions and induce even deposition. **Figure 14. (a)** is the mechanism schematic. In **Figure 14. (b)**, a symmetric cell test assembled by two PANZ@Zn electrode results were shown, PANZ@Zn||PANZ@Zn symmetric cell had a stable cycling life for 1145 h with only 75 mV voltage hysteresis, and in the full batteries test, **Figure 14. (c)**, PANZ@Zn||MnVO lasted longer than the pure zinc full batteries. In order to inhibit side reactions and dendrite growth, a polyvinyl butyral film with high viscoelasticity is applied to the surface of the zinc material by the group of Hao [67]. This film acts as an artificial solid/electrolyte interphase (SEI) and is uniformly deposited on the zinc surface using a straightforward spin-coating approach.
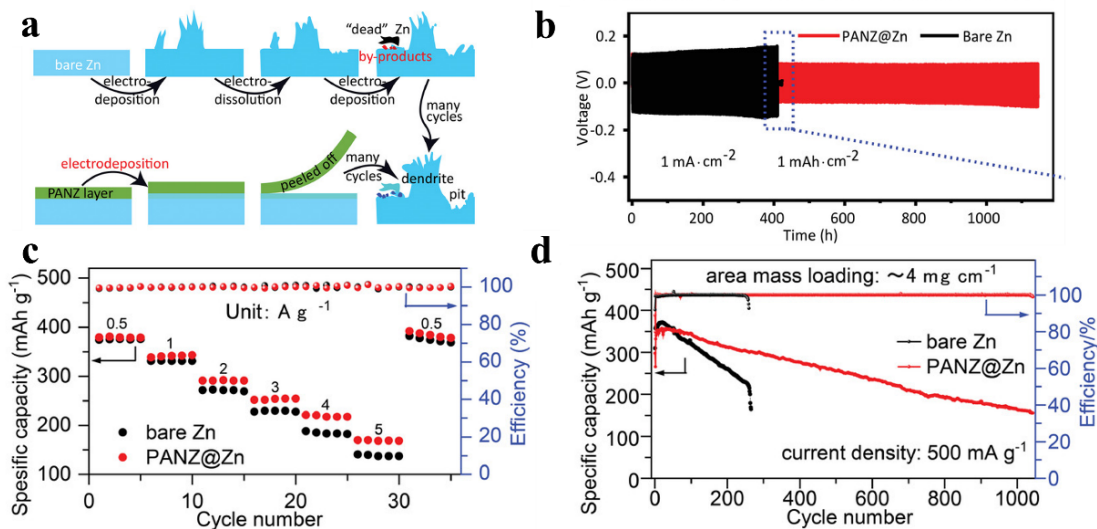
Figure 14. (a)Schematic depiction of the plating/stripping on bare Zn and PANZ@Zn. (b) Bare Zn||bare Zn and PANZ@Zn||PANZ@Zn symmetric cells at 1 mA cm^{-2} with a fixed capacity density of 1 mAh cm^{-2} (c) Rate performance of full batteries. (d) Long-term cycling performance of full batteries. Open access 2021, Wiley

From **Figure 15. (b)**, extremely stable and long symmetrical cycling can be observed of PVB@Zn covered samples. Also, in the full cell test, **Figure 15. (c)**, PVB covered zinc anode performed better, accomplished 1500 cycles under 5C and attained better capacity than pure zinc anode. Here, polypyrrole is exploited by the group of Feng Zhang [68] to manipulate the plating and stripping of Zn^{2+} via the interaction between –NH and Zn^{2+}. This phenomenon results in the growth of zinc microplates in a nearly parallel orientation to the current collector, effectively circumventing any negative effects. As demonstrated in symmetric PPy-coated Zn//PPy-coated Zn (**Figure 16. (a-d)**) and PPy-coated Zn//active carbon systems (**Figure 16. (e)**), the performance of PPy-coated Zn anodes is significantly improved. In **Figure 16. (e)**, the PPy-coated Zn//active carbon system can steadily operate at 5 A g^{-1} for 12,000 cycles while maintaining 96% capacity.

29
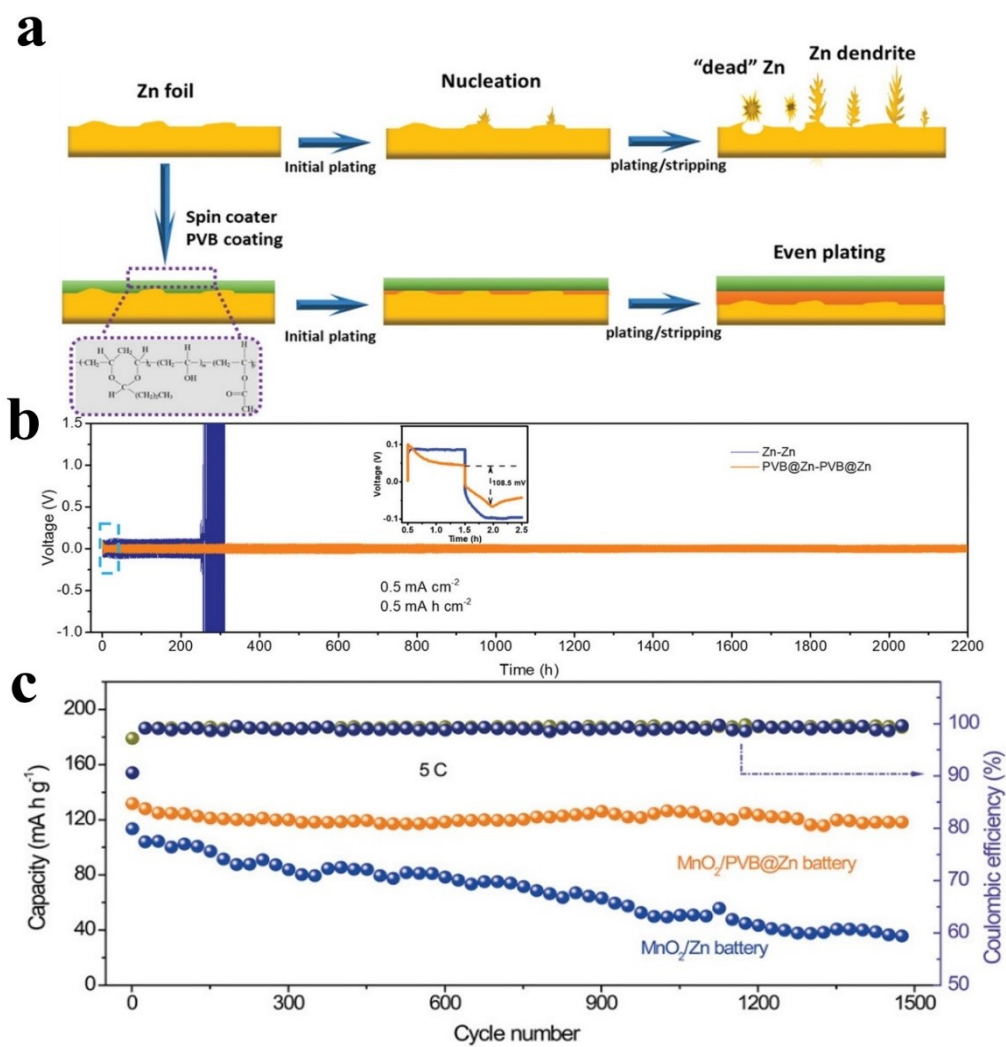
Figure 15. (a) Schematic depiction of the plating/stripping on bare Zn and PVB@Zn. (b) Bare Zn‖bare Zn and PVB@Zn‖PVB@Zn symmetric cells at 0.5 mA cm^{-2} with a fixed capacity density of 0.5 mAh cm^{-2}. (c) Long-term cycling performance of full batteries. Copyright 2020, Wiley
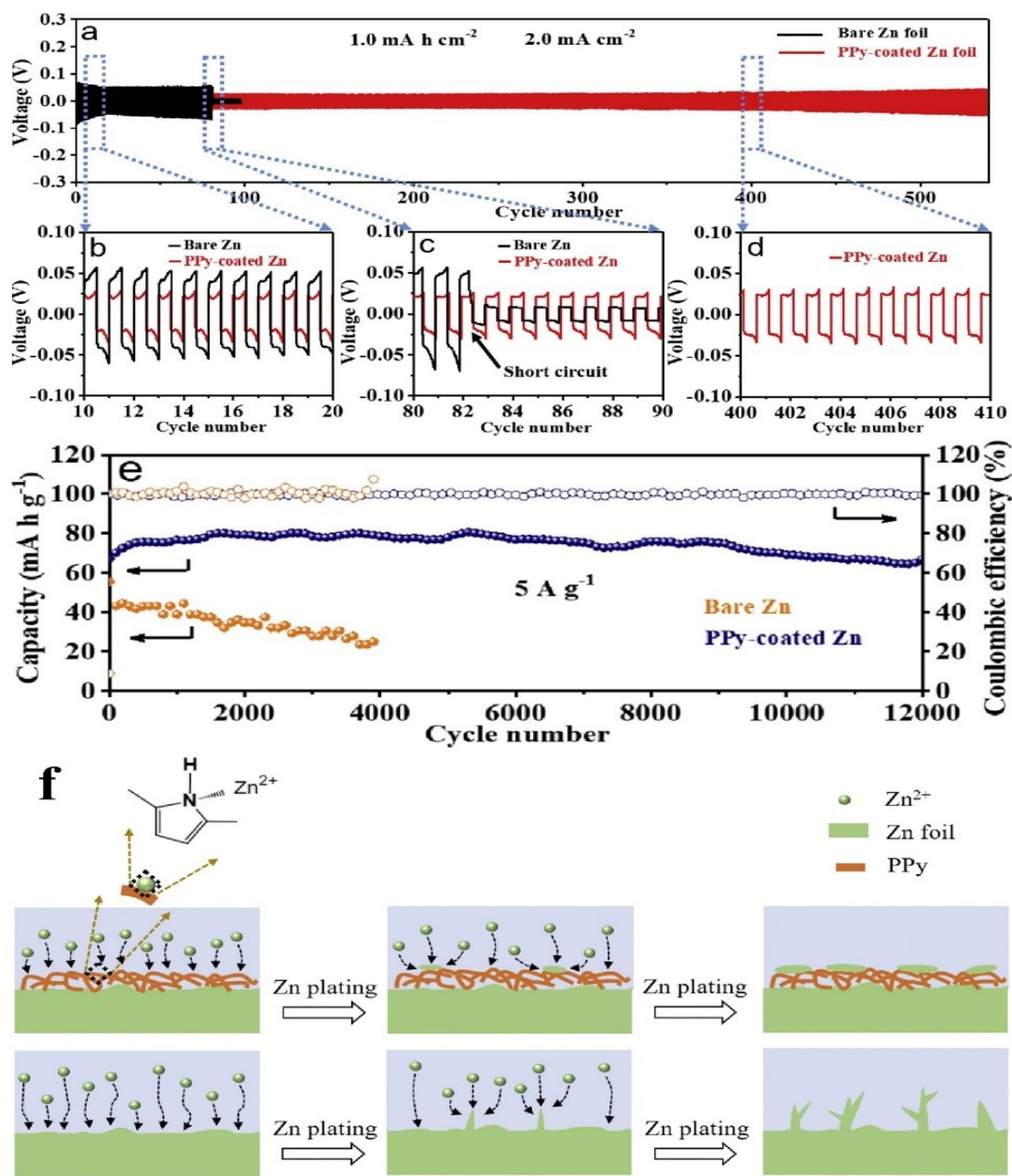
Figure 16. (a) Bare Zn‖bare Zn and ppy@Zn‖ppy@Zn symmetric cells at 2 mA cm^{-2} with a fixed capacity density of 1 mAh cm^{-2}. (b-d) Enlarged voltage profiles at different cycles (e) Long-term cycling performance of full batteries. (f)Schematic depiction of the plating/stripping on bare Zn and ppy covered Zn. Copyright 2020, Elsevier
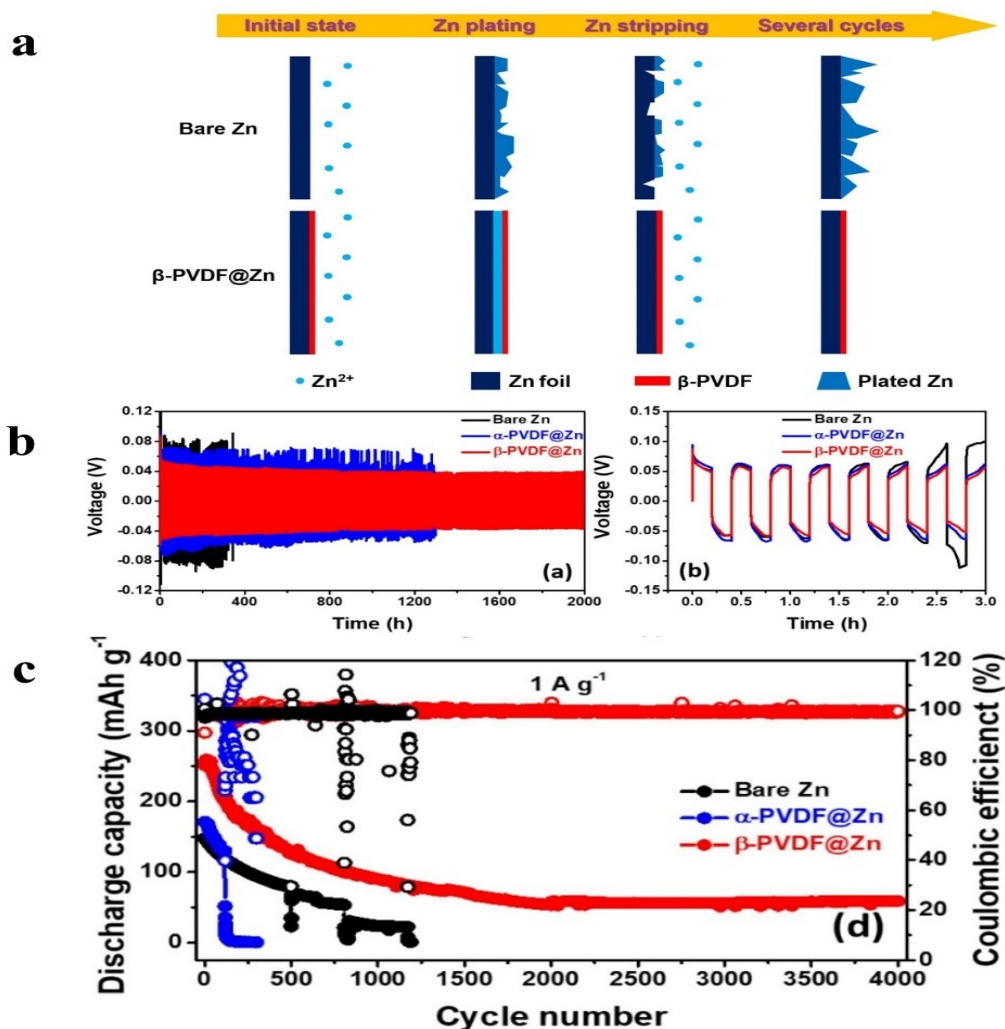
Figure 17. (a) Schematic depiction of the plating/stripping on bare Zn and PVB@Zn. (b) Bare Zn||bare Zn, α-PVDF@Zn||α-PVDF@Zn and β-PVDF@Zn||β-PVDF@Zn symmetric cells at 0.25 mA cm^{-2} with a fixed capacity density of 0.05 mAh cm^{-2}. (c) Long-term cycling performance of full batteries. Copyright 2021, Elsevier

Hieu et al. [52] reported that the β-PVDF layer effectively regulates the Zn stripping/plating process and inhibits corrosion. The results of β-PVDF-coated Zn anode (β-PVDF@Zn) demonstrated superior performance compared to bare Zn metal and α-PVDF@Zn. In a symmetric cell test, β-PVDF@Zn||β-PVDF@Zn obtained a low overpotential of only 40 mV after 2000 hours

of stable operation (**Figure 17. (a)**). Additionally, β-PVDF significantly prolongs the lifespan of the β-PVDF@Zn full cell, with remarkable cyclic stability for up to 4000 cycles (**Figure 17. (c)**). Cao et al. [69] used cyanoacrylate adhesive (502 glue) as the interface of the zinc anode. As a result, this approach achieved stable symmetric cell voltage profiles and a high coulombic efficiency of 99.74% during cycling for the 502-coated Zn//Cu (**Figure 18.** c), which is significantly better than bare Zn anode electrochemical performances.
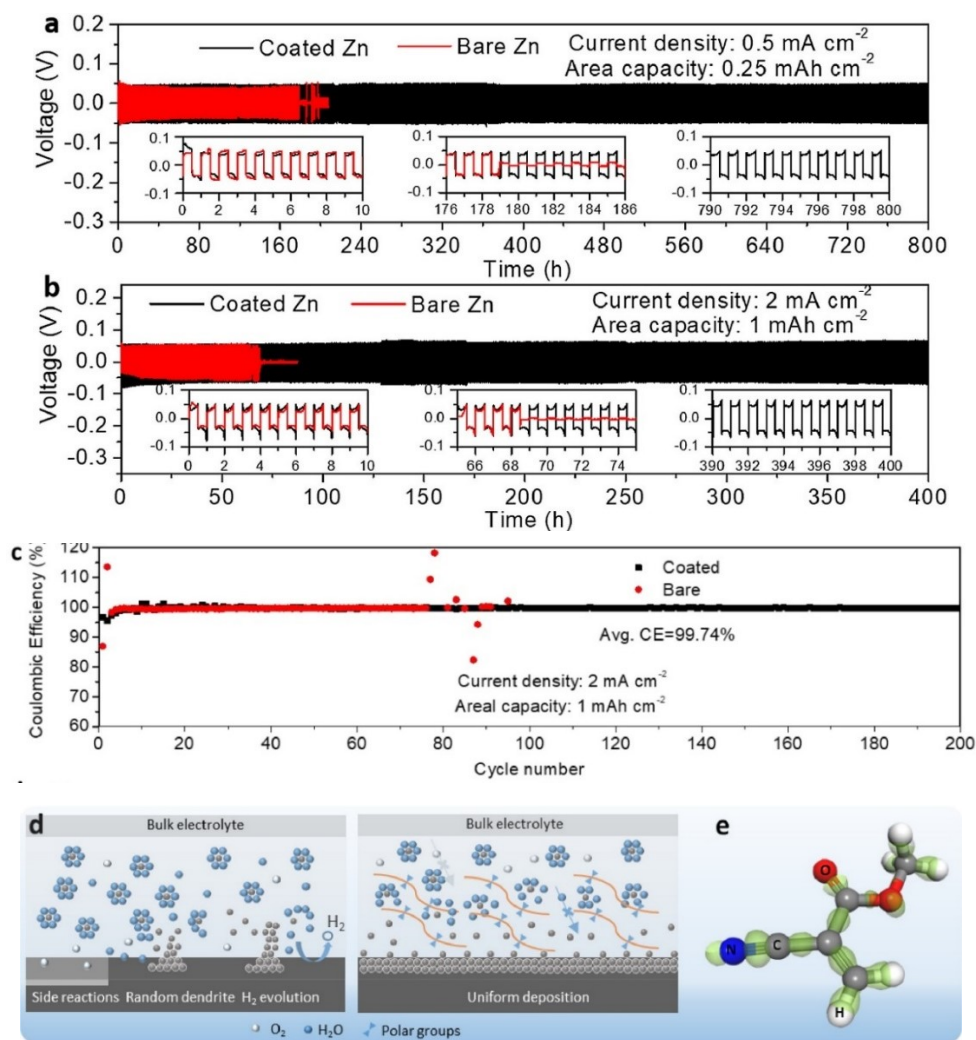
Figure 18. (a-b) The Zn plating/stripping performance for bare Zn foil and 502-decorated Zn foil under various current densities and capacities. (c) Long-term cycling performance of Zn-Cu batteries. (d) Schematic depiction of the 502 coating. Copyright 2021, Elsevier

33

2.4.2 MOFs

Metal organic frameworks (MOFs), by means of its high microporosity and high scalability, received a lot of attention in the artificial interlayer field, such as zeolitic imidazolate framework-8 (ZIF-8) [56,57,58], ZIF-7 [59], *etc.*

Zeng et al. [56] coated ZIF-8 on the surface of the zinc metal anode, as shown in **Figure 19. (a-b)**. **Figure 19. (c)** described the symmetric cell tests of ZIF-8@Zn|| ZIF-8@Zn and Zn|| Zn, the life span of the coated electrode was dramatically more extended than bare Zn, achieved 5000 cycles under a high current density of 10 mA cm^{-2}, capacity density of 1 mAh cm^{-2}. Also, the full battery test of ZIF-8@Zn||α-MnO$_2$, **Figure 19. (d)**, demonstrated the ZIF-8 covered zinc metal anode full battery maintained a discharge capacity of 150 mA h g^{-1} as the capacity retention is 76% after 250 cycles. Liu et al. [57] (**Figure 20. (a)**) also reported that the Zn@ZIF anode showed highly reversible, dendrite-free Zn plating/stripping behavior under different current densities, and a symmetric cell assembled by Zn@ZIF anode can sustain up to 1200 hours with a low polarization at a current density of 2 mA cm^{-2}. Moreover, this ultra stable Zn@ZIF anode enabled a LaVO$_4$//Zn full battery with extremely long cyclic stability and high-capacity retention. (10 000 cycles, 101 % retention).
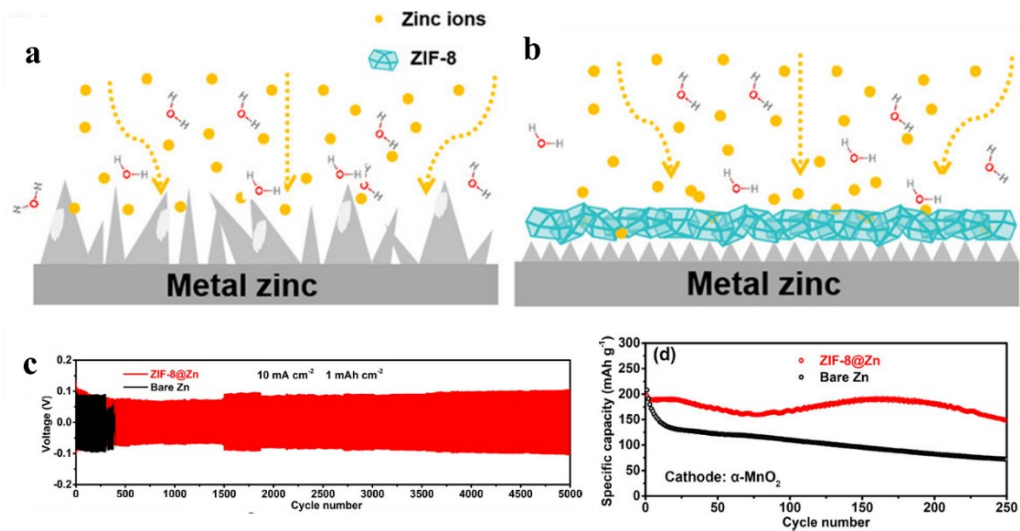
Figure 19. Schematic description of zinc deposition on (a) Zn, (b) ZIF-8@Zn. (c) Cycling performance of symmetric cells 10 mA cm^{-2} and 1 mA h cm^{-2}. (d) Cycling performance of full batteries at 0.5 A g^{-1}. Copyright 2021, American Chemical Society
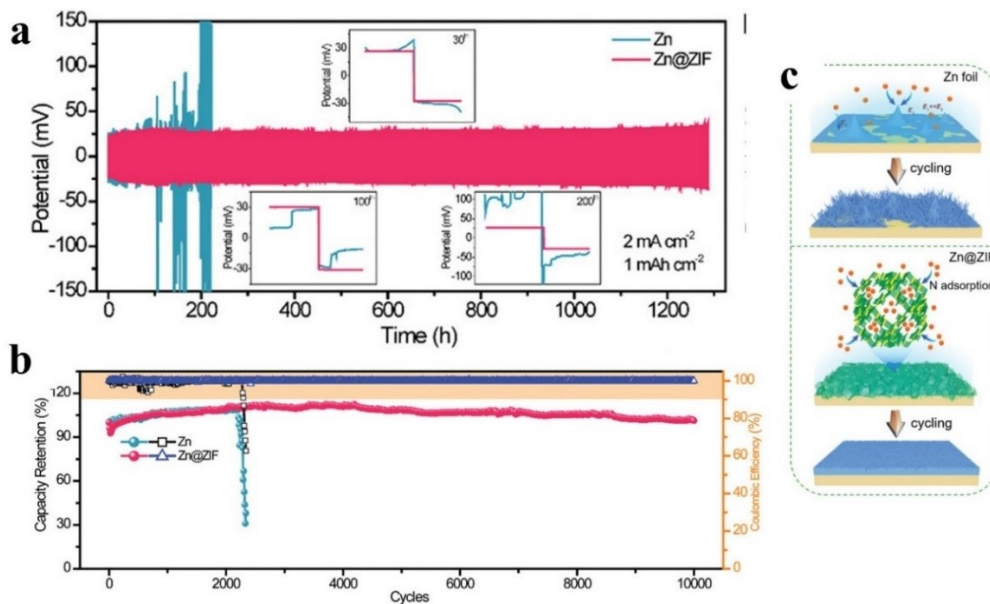
Figure 20. (a) Bare Zn‖bare Zn and Zn@ZIF‖Zn@ZIF symmetric cells at 2 mA cm^{-2}, 1 mAh cm^{-2}. (b) Long-term cycling performance of full batteries. (c) Schematic depiction of the plating/stripping on bare Zn and ZIF coated Zn. Open access 2020, Wiley

35

2.5 Conclusions and Perspective

In conclusion, this review offers a comprehensive summary of the diverse approaches employed in constructing interfacial layers for zinc metal anodes and highlights the recent advancements in surface modifications of zinc metal anodes for achieving high-performance AZIBs. Various coating materials have been discussed, including carbon-based materials, metal oxides, metals and alloys, inorganic acid salts, polymer materials, and MOF-based materials. These coating layers offer several advantages, such as inducing uniform Zn deposition by working as deposition seed; improving zinc ion diffusion pattern by its porosity or zincophilicity; ensuring even distribution of charge across the surface of the zinc anode; inhibiting electrolyte corrosion by acting as an insulating layer.

Despite progress in the surface modification of Zn metal anodes, several challenges remain that need to be addressed. These include paying attention to factors like coating layer thickness, adequate mechanical strength, and strong interfacial bonding. However, tradeoffs are inevitable in current circumstances. (1) Conflict between the conductivity and dendrite suppressing capability. Protective layers made of conductive materials such as carbon-based materials can prevent Zn dendrites from penetrating and lead to the even deposition of zinc ions. However, these layers are not durable, as Zn dendrites can grow from their surfaces, leading to subpar battery performance. On the other hand, insulating layers can act as a stable inert interlayer and prevent corrosion by electrolytes. Nevertheless, these layers can negatively affect electrons and ion transport, resulting in lower battery performance. As a result, finding a solution to overcome these issues that is easy to scale up is necessary. (2) Conflict between the thickness and electrochemical performance. Thicker layers can improve the anode's resistance to corrosion, but the excessive thickness can impede ion diffusion and harm electrochemical performance. Additionally, the coating must possess sufficient mechanical strength and form a strong interfacial bond.

Moreover, most of the research about ion deposition/stripping and dendrites growth patterns is

based on alkaline metal anodes such as Li and Na anodes. Therefore, more simulations, experiments, and theoretical calculations about the basic zinc ion deposition/stripping and dendrites growth pattern are required.

Lastly, it is essential to standardize the zinc anode tests to facilitate practical applications of AZIBs. Current zinc metal anode performance tests normally cannot represent actual use conditions of a practical battery because of the overabundant zinc metal. Furthermore, what key parameters such as CE, CA, symmetric cells lifespan and full cell performances are not negligible should also be determined. In this context, it is crucial to investigate further standardized testing and evaluation criteria to facilitate the practical utilization of AZIBs.

Chapter 3. Methodology

In this chapter, a detailed description will be provided for the systems that are being analyzed. The solution variables and governing equations that will be solved for each system will also be outlined, along with an explanation of the boundary conditions. The governing equations for each system will be fully derived, as they are not readily available in the literature and may not be straightforward. Additionally, the input parameters used in the analysis will be discussed, and an explanation of how the finite element method can be applied to solve the governing equations will be provided.

3.1 X-ray diffraction (XRD)

X-ray Diffraction (XRD) is a nondestructive technique that provides detailed information about the crystal structure, chemical composition, and physical properties of a material. It operates on the principle that the X-rays produced are collimated and directed towards a nanomaterial sample. When the incident X-rays interact with the sample, they undergo scattering, resulting in the generation of diffracted rays. These diffracted rays are then detected, processed, and counted. The intensity of the diffracted rays, scattered at various angles by the material, is plotted to generate a diffraction pattern. This pattern provides valuable information about the atomic arrangement and crystal structure of the sample. A typical XRD diffractometer consists of three main components: an X-ray source, a sample, and a detector.

The qualitative phase analysis involves comparing the diffraction pattern of a material with standard crystallographic databases like the International Center for Diffraction Data (ICDD). This comparison helps in the identification of the phases present in a wide range of crystalline samples, facilitating the phase identification process. By matching the diffraction pattern of the sample with known patterns in the database, the specific phases and crystal structures present in the material

can be determined.

3.2 Scanning Electron Microscope (SEM)

A scanning electron microscope (SEM) is an advanced microscopy technique that uses a focused beam of electrons to generate high-resolution images of a sample's surface. The electrons interact with the atoms in the sample, producing various signals that provide information about the surface topography and composition. The SEM operates by scanning the electron beam across the sample in a raster pattern, and the position of the beam, combined with the intensity of the detected signals, generates an image. The scanning electron microscope mainly consists of the following parts: an electron gun, electromagnetic lens, scanning coils, electron detector, and TV scanner.

3.2 Cyclic Voltammetry (CV)

Cyclic Voltammetry (CV) is a technique used to study the behavior of electrochemical reactions at the electrode - electrolyte interface. In general, it is used to study the electrode reaction mechanism, reaction kinetics, etc. The basic principle of the cyclic voltammetry test is to apply a triangular waveform pulse voltage to the electrodes, the wavelength is shown in **Figure 21**. The initial forward scan (from a to b) involves applying an increasing potential. As a result, the cathodic current, assuming the presence of reducible analytes in the system, will generally increase during this time. Once the reduction potential of the analyte is reached, the cathodic current will begin to decrease as the concentration of the reducible analyte is depleted. If the redox couple is reversible, the subsequent reverse scan (from b to c) will involve the re-oxidation of the reduced analyte. This will generate a current with the opposite polarity (anodic current). The shape of the oxidation peak will closely resemble that of the reduction peak if the redox couple is highly reversible. Therefore, the CV plot can provide information on reversibility and electrochemical reaction from the peaks and information on diffusion kinetic from the reaction current density.

Cyclic Voltammetry Potential Waveform
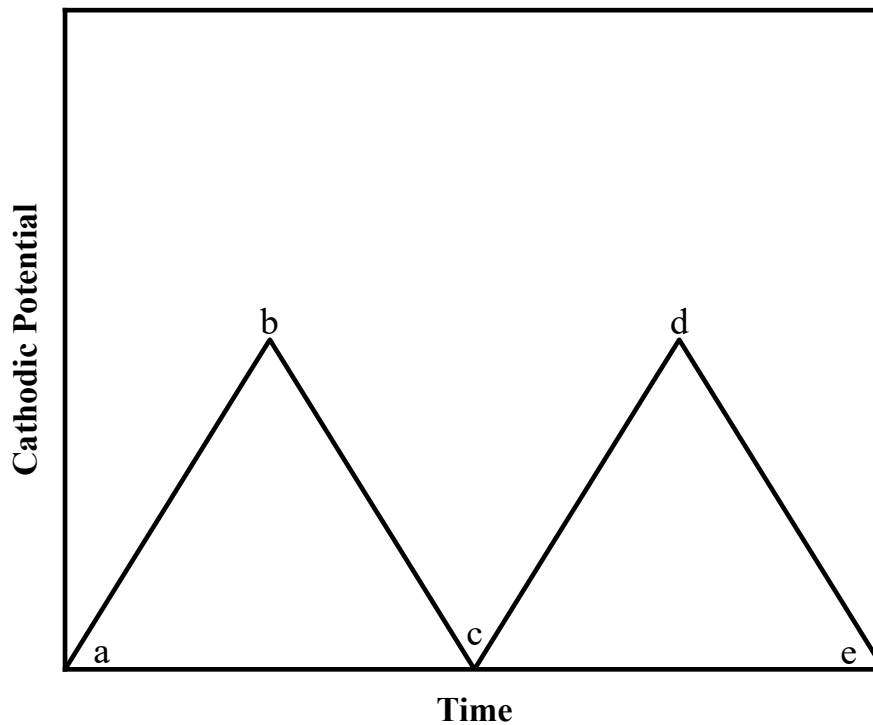
Figure 21. Cyclic Voltammetry Potential Waveform

3.3 Coulombic Efficiency (CE)

Coulombic Efficiency (CE) represents the capacity retention during each charge/discharge cycle.
The less capacity loss during cycling, the higher the CE and the longer the cycling life of batteries.
In zinc ion batteries, it could be written as:

$$CE = \frac{Number\ of\ Zn^{2+}\ intercalated\ in\ cathode}{Number\ of\ Zn^{2+}\ departed\ from\ cathode}$$

A poor CE is caused by the side reaction on the zinc anode's surface, which was indicated in
section 1.2. Therefore, CE is a parameter for analyzing the reversibility in zinc ion batteries.

3.4 Symmetric Cell Analysis

In order to obtain accurate and vast information about reactions between electrode and electrolyte, symmetric cells with two Zinc plate electrodes. Although the cells have an average voltage of zero volts and no practical usage, in the investigation of electrode reversibility, electrode potential profile, the symmetric has an undeniable position and is intensively applied worldwide. In my project, several test circumstances used symmetric cells as test samples and received multiple graphs that possess information about the cell performance. I will discuss them in the following paragraphs.
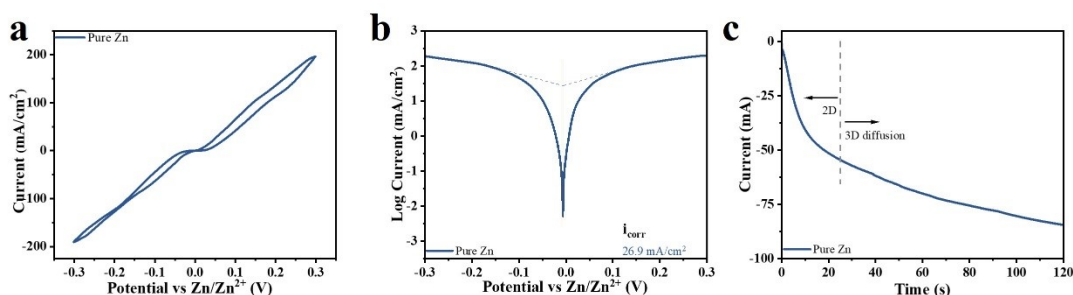
Figure 22. (a) Cyclic voltammetry (CV) results of the assembled symmetric cells; (b) Linear polarization curves of coated or bare Zn; (c) Chronoamperograms of coated Zn or bare Zn.

These graphs are drawn based on the data tested by the electrochemical workstation (Bio-Logic electrochemical workstation). **Figure 22. (a)** is the cyclic voltammetry (CV) result of the symmetric cells. The obligation of this graph is to show the activity of Zn^{2+} on the deposition interface and reflect the deposition speed of Zn^{2+} by the cumulative area inside the CV curve; the larger the area is, the faster the deposition and activate more nucleation sites for Zn^{2+} deposition [95]. **Figure 22. (b)** is the linear polarization curve derived from **Figure 22. (a)** by replacing the y-axis with the Log current. The obligation of this graph is to testify and compare self-corrosion rate and anode dissolution; the metrics of this graph are (1) Horizontal position of the tip of curves,

the more positive potential mains, the lower corrosion potential. (2) The corrosion current can be located at the intersection of corrosion potential and extension of the linear part, the lower the corrosion current indicates a lower corrosion rate. **Figure 22. (c)** is the Chronoamperograms (CA) of the samples generated by applying a negative overpotential of -150 mV to the symmetric cell. The purpose of this test is to investigate the diffusion pattern of the interested electrode. According to the **Figure 22. (c)**, a curve can be divided into two parts, 2d diffusion and 3d diffusion. The steep 2d diffusion part indicates the growth of Zn dendrite because the Zn ions deposit along the favorable nucleation sites with the lowest energy as the 3d diffusion line shows that the Zn ions deposition is restricted and suppresses the dendrite growth, and the increasing current of 3D diffusion part is caused by the increasing area of the electrode due to dendrite growth [84, 111, 116].

The following graphs are drawn based on the test results using a Neware Battery Measurement System (Neware, China), **Figure 23. (a)** is the rate performance of the symmetric cells under different current densities. The primary purpose of the rate performance test is to reveal the charge/ionic motion in the electrode and electrolyte in timescale [44]. Among these curves, if the curve has a bigger gap between the positive and negative voltage in one cycle, it means it has a larger overpotential which is not desirable, caused mainly by the high impedance of the cell. **Figure 23. (b)** shows the exchange current density of samples calculated by the function [101] of

$$i \approx$$

$$i_0 \frac{2F\eta}{RT} \tag{5}$$

where i is the running current density, i_o is the exchange current density, F and R, are Faradic and gas constant, respectively. T is temperature, and η is total overpotential, as a higher exchange current density indicates a higher deposition kinetic[101]. The function (5) is the Bulter-Volmer equation at the low overpotential region because the overpotential under 150 mV can be defined as a low overpotential region. Here I will show the derivation process of (5)

$$i \approx i_0 \{ \exp \left[\frac{2\alpha_a F \eta}{RT} \right] -$$

$$\exp \left[-\frac{2\alpha_c F \eta}{RT} \right] \} \qquad (6)$$

where α_a is the anodic charge transfer coefficient, and α_c is the cathodic charge transfer coefficient, while the

$$\frac{F\eta}{RT} \ll 1 \qquad (7)$$

$$\alpha_a + \alpha_c = 1 \qquad (8)$$

function (6) can be simplified into

$$i \approx i_0 \{ \frac{2\alpha_a F \eta}{RT} + \frac{2(1-\alpha_a)F \eta}{RT} \} \qquad (9)$$

then simplify the function (9), can receive

$$i \approx$$

$$i_0 \frac{2F\eta}{RT} \qquad (5)$$

Figure 23. (c) is the long-term cycling of symmetrical cells, which can intuitively present the reversibility of electrodes in time scale and can show the change of overpotential during the long-time cycling. The longer cycling with lower and more stable overpotential are desired properties of the electrode.
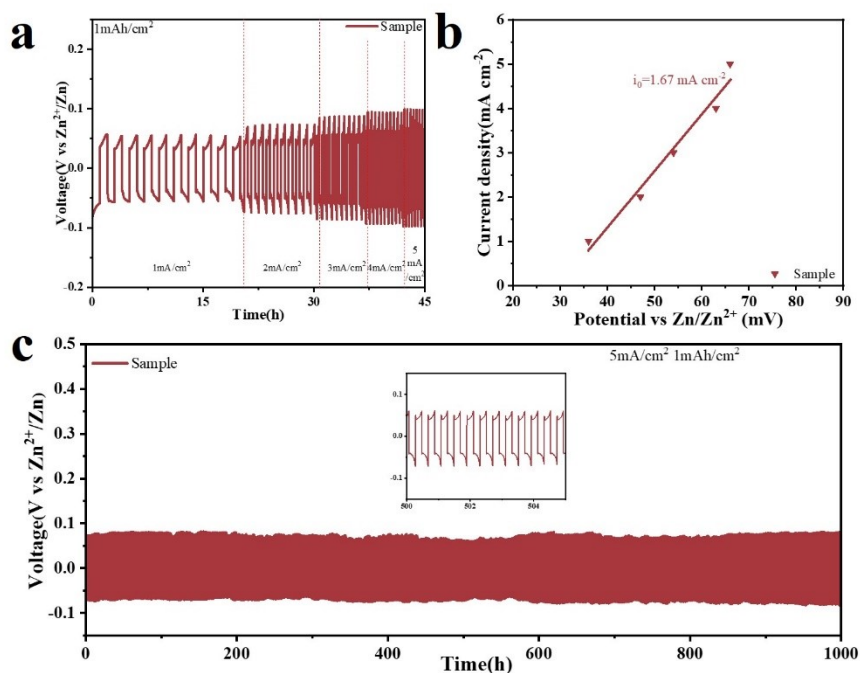
Figure 23. (a) Rate performance of the symmetric cells at 1,2,3,4 and 5 mA cm^{-2}; (b) Plots of the potential-current density of the symmetric cells; (c) Long-term cycling of symmetrical cell using bare or coated Zn

3.5 Half Cell Analysis

Battery chemistry is typically evaluated through the use of half cells, which consist of a working electrode paired with a reference electrode that maintains a constant potential during operation. A counter electrode is also included in the half cell, which functions solely to carry the current flowing through the cell. In the project, Cu foil was used as the reference electrode to investigate the electrode reversibility and electrode potential profile. The meanings of the received graphs will be discussed in the following paragraphs.

Figure 24. (a) is the Coulombic efficiency (CE) graph of the half cell, which is crucial for the evaluation of the reversibility of the anode. The coulombic efficiency is the ratio of discharge

capacity and charge capacity. A half cell with a near 100% CE and longer lifespan means the half cell has better reversibility. **Figure 24. (b)** is the voltage profile of the half cell. This graph describes the areal capacity and voltage relationship at a specific cycle of the CE graph (**Figure 24. (a)**). The primary purpose of this graph is to identify the voltage polarization. Voltage polarization is a term that refers to the potential to activate the reaction; the larger the voltage polarization indicates, the harder the deposition will be achieved. **Figure 24. (c)** is the CV test for Zn nucleation on Cu foil. In the graph, the difference between points a and b is the nucleation overpotential, as a bit higher nucleation overpotential means finer nucleai and restriction of tip effect [45].
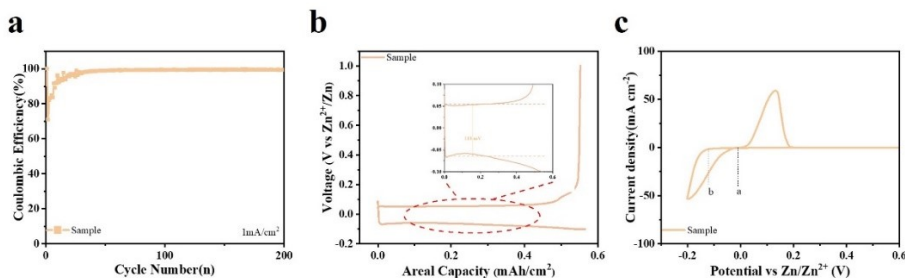
Figure 24. (a) CE test example; (b) Comparison of charge-discharge curves at 50th cycle from CE test; (c) CV test for Zn nucleation on Cu foil.

3.6 Full Cell Analysis

The full-cell configuration consists of both a negative electrode and a positive electrode, both of which are used as the working electrode. This configuration is highly relevant and promising for use in realistic battery systems and has therefore been frequently utilized to predict the performance of new battery chemistries in practical applications. In this project, V_2O_5 is used as cathode material to investigate the full cell performance.

Figure 25. (a) is the CV profiles of full cells, the position of the reduction peak assigned to the insertion of Zn ions for the formation of $Zn_xV_2O_5$, as the oxidation peak is the sign of the Zn^{2+} and

H$^+$ extraction. **Figure 25. (b)** is a sample of the galvanostatic cycling performance of full cells. The attention required points are the capacity curves, each curve describes a trend of capacity change along the time, and coulombic efficiency points, each point represents the charging efficiency of each cycle. **Figure 25. (c)** is a galvanostatic charge/discharge (GCD) profile. From this profile, the polarization voltage can be identified, the gap between charging and discharging curves. The less polarization voltage means better performance. **Figure 25. (d)** is the rate performance of full cells. This test can show the capability of charging or discharging capability under different current densities. A good rate performance should have high capacity at any current density; some article declares that it may be related to the restriction of side reactions [46].
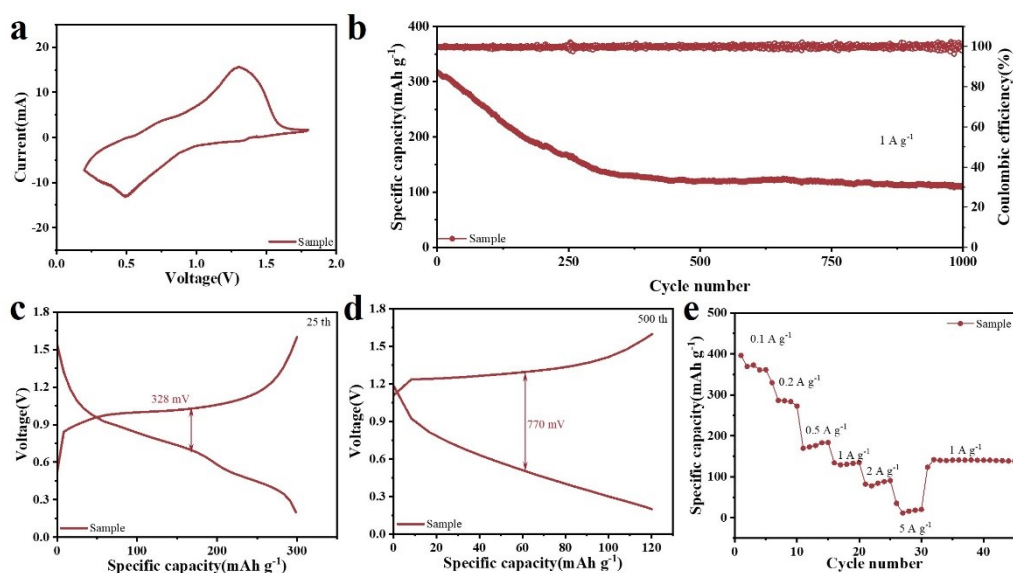
Figure. 25 (a) CV profiles of full cells for 1st cycle; (b) Galvanostatic cycling performance of full cells at 1 A g^{-1}; Galvanostatic charge/discharge profiles at (c) 25th cycle and (d) 500th cycle; (e) Rate performance tested under different current densities.

Chapter 4. Synergistic Artificial Interlayer to Enhance the Homogeneity of Zinc-ion Flux for Dendrite-free Zinc Metal Anode

Abstract

Compared with Li-based batteries, aqueous zinc ion batteries (AZIBs) illustrate great promise in large-scale energy storage ascribed to their high safety and low cost. However, the inhomogeneous growth of zinc dendrites and electrolyte corrosion on the zinc (Zn) metal anode severely hinder the practical application of ZIBs. Herein, we proposed a simple, effective artificial interface coating by integrating the 2D g-C_3N_4 nanosheets with 3D ZIF8 nanoparticles (g-C_3N_4@ZIF8) to enhance Zn anode reversibility. The ZIF8-supported g-C_3N_4 can not only regulate the Zn-ion flux but also rapidly transfer the charge to deposit on the Zn surface, which leads to a boosted electrochemical performance. Thus, a dendrite-free Zn anode with an ultralong cycling lifespan of up to 4,400 h and superior rate capability is achieved. Furthermore, when coupled with the V_2O_5 nanopaper cathode, the assembled AZIBs exhibits a long-term span over 1,000 cycles at 1 A g^{-1}. This work provides a more simplistic and efficient strategy for building a dendrite-free and long-lasting protecting layer for Zn metal.

4.1. Introduction

Due to the shrinking fossil fuel storage and rapid growth of environmental concerns, the exploration of green and sustainable electrochemical energy sources for large-scale energy storage is urgently needed. Compared with the safety hazards and economic challenges in popular Li-ion batteries (LIBS), aqueous Zn-ion batteries (AZIBs) are regarded as one of the most promising candidates for the next future grid-scale energy storage, owing to their high safety level, low cost, and environmentally friendly. More importantly, AZIBs can enhance their energy density by utilizing metallic Zn directly as the anode due to their high theoretical capacity (820 mAh g^{-1}[1]/ 5854 mAh cm^{-3}). In addition, Zn's low redox potential (-0.76 V vs SHE [70]) makes it more stable in water-based electrolytes compared to Li (the redox potential of lithium is -3.04 V vs SHE[71]). However, AZIBs have several fatal shortcomings, including inferior cathode performance, weak separator strength, and failure of the Zn anode[72]. Among these issues, metal anode failure, caused by dendrite growth, passivation, and corrosion of pristine Zn in electrolytes[72], is commonly considered a major factor in AZIB failure.

The dendritic Zn is usually formed from unevenly distributed Zn^{2+} flux near the surface of the anode with random nucleation, which will further introduce the so-called "tip effect" [73-75]. Hence, the preferential deposition at the Zn-tip is the primary reason for zinc-dendrite. Based on this point, extensive efforts have been devoted to achieving a highly stable Zn metal anode, such as designing a novel structure for the Zn anode[76], interfacial engineering[77], or introducing electrolyte additives [78]. Constructing a 3D conductive host is usually considered an effective strategy due to the porous framework with an enlarged effective specific surface area which can not only reduce local current densities and suppress the formation of large dendrites but also buffers the volume expansion during Zn plating [79]. Nevertheless, as nucleation sites increase, hydrogen evolution and corrosion reactions are also more likely to happen[80]. Electrolyte additives have been widely reported as effective methods to regulate Zn^{2+} flux or reduce the active

molecules in solvated ions. However, the additional extra cost of these additives is a potential disadvantage [72]. In comparison, a functional interlayer that is inertia and allows for even Zn^{2+} penetrability can not only regulate the Zn^{2+} flux but also inhibit side reactions between the electrolyte and Zn electrode. As a result, the construction of the functional interlayer is one of the most effective and promising methods.

So far, to achieve highly reversible Zn metal anodes, zincophilic materials (such as Cu [81], Sn [82], N-doped monolayer graphene [83], conductive graphite (KS-6) [84], g-C_3N_4[85], *etc.*) are widely applied due to their absorb/bonding ability of nuclear sites to Zn^{2+}[85, 86]. Among them, the Zn-N bond has been reported to induce even deposition on the carbon host and suppress zinc dendrite formation[87]. Herein, 2D graphitic carbon nitride (g-C_3N_4) is one of these kinds of materials that possesses a nanosheet structure with apertures[88]. Yang *et al.* reported a technique of deploying g-C_3N_4 on the separator to regulate zinc ion flux and achieved longer durability. Additionally, the individual g-C_3N_4 nanosheet exhibits a high shear modulus of ~21.6 Gpa originating from the strong covalent in-plane interaction, which can further enhance the potential tolerance of volume changes [89]. However, with a dielectric constant of 7-8 [90], g-C_3N_4 possesses a large amount of static electricity, which may cause uneven deployment and restacking on the surface of the Zn electrode, leading to uneven Zn deposition. Moreover, zeolitic imidazolate framework-8 (ZIF8) with a regular 3D porous structure has recently been utilized as an effective functional material to regulate Zn^{2+} diffusion, nucleation, and deposition behaviors, further refraining from the "tip effect"[91]. Additionally, MOF-type nanoparticles exhibit superior hydrophilicity and can adsorb electrolytes in extremely small spaces, resulting in both nano-level wettability and uniform Zn^{2+} flux over the Zn anode[92]. Furthermore, ZIF8 has a much lower dielectric constant of 2-3 compared to g-C_3N_4[93]. Yuan *et al.* reported that g-C_3N_4@ZIF8 can separate the g-C_3N_4[94] to lower the impedance by avoiding restacking of g-C_3N_4. Therefore, the combination of g-C_3N_4 and ZIF8 is believed to be a promising strategy to tackle the drawbacks of the Zn anode.

Herein, a simple, effective artificial interface coating is achieved by integrating the 2D g-C_3N_4 nanosheets with 3D ZIF8 nanoparticles (g-C_3N_4@ZIF8), which is a specially designed multidimensional nanostructure to enhance Zn anode reversibility.   g-C_3N_4 sustained by ZIF8 can modulate and adjust the Zn^{2+} flux, leading to a reduction in the corrosion area of the zinc anode in water-based electrolyte. Additionally, with the low conductivity of g-C_3N_4 and ZIF8, Zn^{2+} can only migrate through the interlayer and deposit between the interlayer and Zn under the external electrical field. With this effective interlayer coating on the Zn anode, the symmetric cell can achieve 4,400 hours of cycling at 0.25 mA cm^{-2}/0.25 mAh cm^{-2} and 1,000 hours of cycling at 5 mA cm^{-2}/1 mAh cm^{-2}, with remarkable rate performance that can reach 40 mA cm^{-2}. When coupled with a flexible V_2O_5 nanopaper cathode, the full cell exhibits the ability to achieve over 1,000 stable cycles at a rate of 1A g^{-1}. Hence, an artificial interlayer on the Zn anode can weaken corrosion and suppresses dendrite growth by evenly distributing ions and electrons, mitigating and slowing down the formation of the non-uniform anode surface. This design deaccelerates the growth speed and reduces the number of dendrites, enabling reversible Zn stripping/plating.

4.2. Experimental Section

4.2.1. Synthesis of g-C$_3$N$_4$

To prepare the sample, 3g of urea was ground and dried at 60 °C for 1 hour. The resulting powder was then collected in a 5 ml quartz crucible and sealed with aluminum foil. The crucible was heated to 550 °C at a heating rate of 5 °C in a furnace in the presence of air. The sample was kept at 550 °C for 2 h and then allowed to cool naturally to 20 °C. Finally, g-C$_3$N$_4$ was obtained.

4.2.2. Synthesis of ZIF8 and g-C$_3$N$_4$@ZIF8

A solution was prepared by dissolving and dispersing 0.219 g of zinc acetate (ZnAc$_2\cdot$H$_2$O) and 30 mg of g-C$_3$N$_4$ in 25 ml of methanol using ultrasonic for 30 minutes. This solution was labelled as solution 1. In a separate container, 0.656 g of 2-methylimidazole (2-MIM) was dissolved in 25 ml of methanol to form solution 2. Solution 2 was then added to solution 1 with stirring for 2 hours. The resulting mixture was allowed to settle for 24 hours at ambient temperature. After that, the pale-yellow solid was collected by centrifugation and cleaned with methanol to remove any unreacted ions and 2-MIM. The final product, g-C$_3$N$_4$@ZIF8, was obtained by drying the collected sample at 60 °C in the oven. To synthesize ZIF8, the same procedure was followed as for g-C$_3$N$_4$@ZIF8, but without adding g-C$_3$N$_4$ to the solution.

4.2.3. Synthesis of V$_2$O$_5$ Nanopaper Cathodes

70mg commercial V$_2$O$_5$ powder (Sigma-Aldrich) and 20 mg CNT was dissolved in 100 mL of 2M NaCl (Fisher Chemical) solution. The solution was sonicated for 10 mins and vigorously stirred for 72 h at room temperature. After 72h, the solution was filtered and washed with water. The film was freeze-dried for 24 h to form a flexible free-standing paper. For the electrochemical test, the free-standing paper was cut into a small disk (1.13 cm^2). The weight of each electrode is around

6.2 mg cm^{-2}.

4.2.4. Fabrication of Batteries and Electrochemical Measurements

To prepare the electrodes, a slurry of the different samples (ZIF8, g-C$_3$N$_4$, and g-C$_3$N$_4$@ZIF8) was created by mixing with PVDF at a weight ratio of 9:1 and dissolving in NMP. Each electrode was coated with 0.44 mg cm^{-2} of the slurry mixture. In the asymmetrical cell configuration, either bare Cu or coated Cu foil was used as the cathode, while coated Zn or bare Zn plates served as counter electrodes. The electrolyte used was 80 µl of 3 M ZnSO$_4$, with glass fiber acting as the separator. The full cell consisted of a V$_2$O$_5$ cathode, a coated or bare Zn plate as the anode, and glass fiber as the separator. The cells were assembled in CR2032 coin cells in an air atmosphere.

The galvanostatic discharge-charge process was measured using a Neware Battery Measurement System (Neware, China), while EIS testing was conducted using a Bio-Logic electrochemical workstation with a frequency range of 10^{-1}-10^6 Hz.

4.2.5. Characterization

The X-ray Diffraction (XRD) patterns were obtained using a Rigaku Ultima IV diffractometer with Cu Kα as the X-ray source. Micro and nanoscale structures were evaluated using a Zeiss EVO M10 scanning electron microscope (SEM), while a Zeiss Sigma field-emission scanning electron microscope (FESEM) coupled with Oxford Instruments energy dispersive x-ray analysis (EDX) was also used.

4.2.6. Computational Method

First-principles calculations were performed using density functional theory (DFT) implemented in the Vienna Ab initio Simulation Package (VASP). The Perdew-Burke-Ernzerhof (PBE) exchange-correlation functional with the Generalized gradient approximation (GGA) was

employed.[95] The plane-wave energy cutoff was considered to be 450 eV with the EDIFF of 1×10^{-6} eV. For the model of Zn atom adsorbed on g-C_3N_4 (001), the $2 \times 4 \times 1$ supercell model was calculated, while the structure was based on previous research.[120] And for the model of Zn atom adsorbed on ZIF8, the unit cell was calculated. The k-point mesh adopted is $1 \times 1 \times 1$ for the ZIF8 model and $3 \times 2 \times 1$ for the g-C_3N_4 model. The vacuum layer of g-C_3N_4 was created to 20 Å, while the ZIF-8 six-membered ring was located in a cubic cell with a side length of 30 Å. The adsorption energy (E_{ads}) for each model was defined as follows:

$E_{ads} = E_{total} - E_{sub} - E_{Zn}$

where E_{total} and E_{sub} are the total energy of the model bound with and without Zn, and E_{Zn} is the energy of the Zn atom.

4.3. Results and Discussion
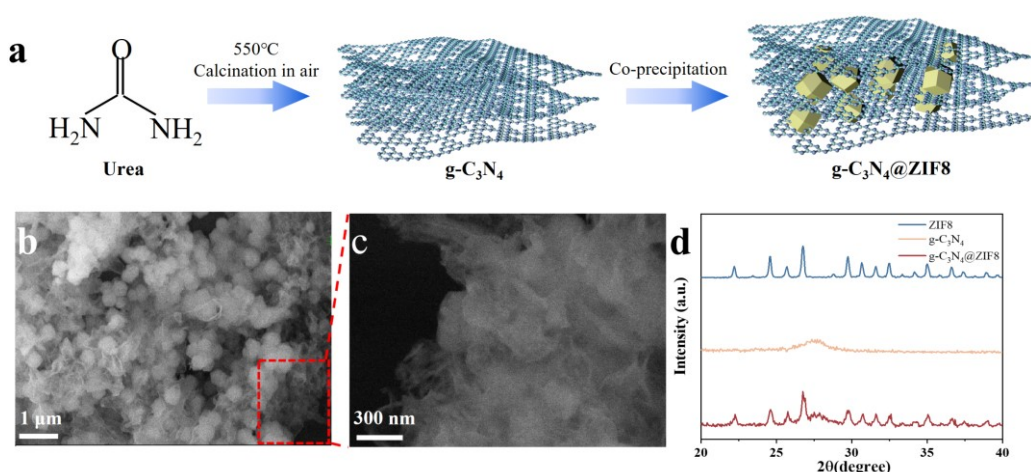
Figure 26. (a) Schematic illustration of preparing g-C$_3$N$_4$@ZIF8; (b-c) SEM image of g-C$_3$N$_4$@ZIF8. (d) XRD pattern of ZIF8, g-C$_3$N$_4$, and g-C$_3$N$_4$@ZIF8.

Figure 26. a indicates the process of synthesizing g-C$_3$N$_4$@ZIF8 involves two steps. In the first step, g-C$_3$N$_4$ is produced from the pyrolysis of urea, resulting in a two-dimensional(2D) nanosheet structure. In the second step, g-C$_3$N$_4$ nanosheets are dispersed in methanol using ultrasonic mixing and then combined with zinc acetate. The addition of 2-Methylimidazole methanol solution triggers the growth of ZIF8 crystals, which then envelop g-C$_3$N$_4$ in the nucleation process to form the g-C$_3$N$_4$@ZIF8. The SEM images in **Figure 26. b** and **Figure 26. c** demonstrate that the ZIF8 nanoparticles have a uniform tetra-decahedron structure and are evenly dispersed on the 2D g-C$_3$N$_4$ nanosheets, with dimensions around 300 nm and no visible vacancies. This self-supported structure enhances the regulation of zinc ion flux to the surface of the zinc anode. The X-ray diffraction patterns are in **Figure 26. d** display the successful integration of g-C$_3$N$_4$ and ZIF8 in g-C$_3$N$_4$@ZIF8, with each peak on the g-C$_3$N$_4$@ZIF8 appearing at the same located degree as the peaks in ZIF8 and g-C$_3$N$_4$. Moreover, the universal reference XRD PDF cards are unavailable for the g-C$_3$N$_4$ and ZIF8 because of the diversity of the g-C$_3$N$_4$ and ZIF8 synthesis processes [123-

124]. Therefore, the identification of the g-C$_3$N$_4$@ZIF8 structure can only be made among the previous papers [125-126], and my sample of g-C$_3$N$_4$@ZIF8 showed the typical XRD pattern consistent with previous reports, confirming the successful preparation of crystalline g-C$_3$N$_4$@ZIF8. The SEM images of Zn foil after coating these materials are depicted in **Figure 27. (a-c)**. They reveal that the g-C$_3$N$_4$@ZIF8 (**Figure 27. a**) attached to the Zn surface shows no cracks or voids. In comparison, the g-C$_3$N$_4$ (**Figure 27. b**) and ZIF8 (**Figure 27. c**) coating layers show plenty of cracks with a non-flat surface. Also, the cross-sectional SEM is shown in **Fig. S1**, which can be observed that the g-C$_3$N$_4$@ZIF8 is evenly distributed on the surface of the Zn anode and superdense than that of g-C$_3$N$_4$ and ZIF8. The contact angle measurement is the way to examine the hydrophilicity of g-C$_3$N$_4$@ZIF8 to 3M ZnSO$_4$ electrolyte, as shown in **Fig. S2**, the contact angle of the bare Zn is 87.25° as the contact angle of the g-C$_3$N$_4$@ZIF8 covered Zn is 74.46°, which implies that the hydrophilicity of g-C$_3$N$_4$@ZIF8 covered Zn is better than pristine Zn due to the coating layer.

To further investigate the performance of g-C$_3$N$_4$@ZIF8 as the protection layer on Zn, batteries were assembled. Coulombic efficiency (CE) is crucial for the evaluation of the reversibility of the anode. **Figure 27. d** shows the CE results of bare Zn and coated Zn anodes. Zn/g-C$_3$N$_4$@ZIF8 indicates longer sustainability than the other samples and better stability, maintaining a high CE of 99.61% for 200 cycles at 1 mA cm^{-2}, 0.5 mAh cm^{-2}. As a comparison, bare Zn can perform 60 cycles, g-C$_3$N$_4$ only maintains 50 cycles and ZIF8 sustains 126 cycles respectively. **Figure 27. e** proves that the estimated voltage polarization of g-C$_3$N$_4$@ZIF8 is 92 mV, which is smaller than the 118 mV observed for g-C$_3$N$_4$ and is comparable to that of ZIF8. Hence, better sustainability of g-C$_3$N$_4$@ZIF8 is demonstrated. As shown in **Figure 27. f**, the shape of the cyclic voltammetry (CV) curves for symmetrical cells is similar, which suggests that the coated electrode and the bare Zn electrode undergo the same electrochemical reaction during Zn stripping/plating process. But the cumulative area of the Zn/g-C$_3$N$_4$@ZIF8 anode is larger than that of Zn/ZIF8 and Zn/g-C$_3$N$_4$, indicating that the g-C$_3$N$_4$@ZIF8 protective layer enhances the activity of the Zn^{2+} deposition

interface and promotes the rapid transfer of Zn^{2+}[95]. This results in the accumulation of more Zn^{2+} and the activation of additional nucleation sites for Zn^{2+} deposition. Moreover, **Figure 27. g** is the linear polarization curve to analyze the self-corrosion rate and anodic dissolution. Among the four tested samples, Zn/g-$C_3N_4@ZIF8$ shows the lowest corrosion current density of 6.05 mA cm^{-2}, which indicates a lower trend of corrosion [96-99]. The nucleation mechanism of Zn^{2+} on g-$C_3N_4@ZIF8$ is further evaluated. As shown in **Figure 27. h**, the CV curves demonstrate the nucleation behavior using bare Zn coupled with Cu foil coated by various samples. A higher nucleation overpotential is typically associated with the formation of finer and smaller Zn-deposited particles [100]. In the case of g-$C_3N_4@ZIF8$, the highest nucleation overpotential is observed, indicating the formation of the smallest and finest nuclei. In addition, the chronoamperometry (CA) curves are shown in **Figure 27. i** further exhibit the intrinsic mechanism of Zn nucleation and growth. A negative overpotential of -150 mV within 120 seconds is applied to the assembled symmetric cells. For the bare Zn, the current density keeps increasing over 120 s, while those of coated Zn reach the maximum current densities within a short time and remain stable for the rest of the time. In detail, the increasing current represents a 2D diffusion process, indicating that Zn ions are inclined to accumulate and form dendrites, known as the "tip effect." And for a stable current, it represents a 3D diffusion process, implying that Zn ions must overcome an additional energy barrier to deposit on the surface of Zn in a confined manner, meaning they must penetrate the coating layer before reducing on the surface of the Zn anode, resulting in a dendrite-free anode. The flatter the curve, the more Zn ions are preferred to reduce nearby instead of diffusing to other sites. Hence, the g-$C_3N_4@ZIF8$ coating layer can lead to a more uniform deposition of Zn.
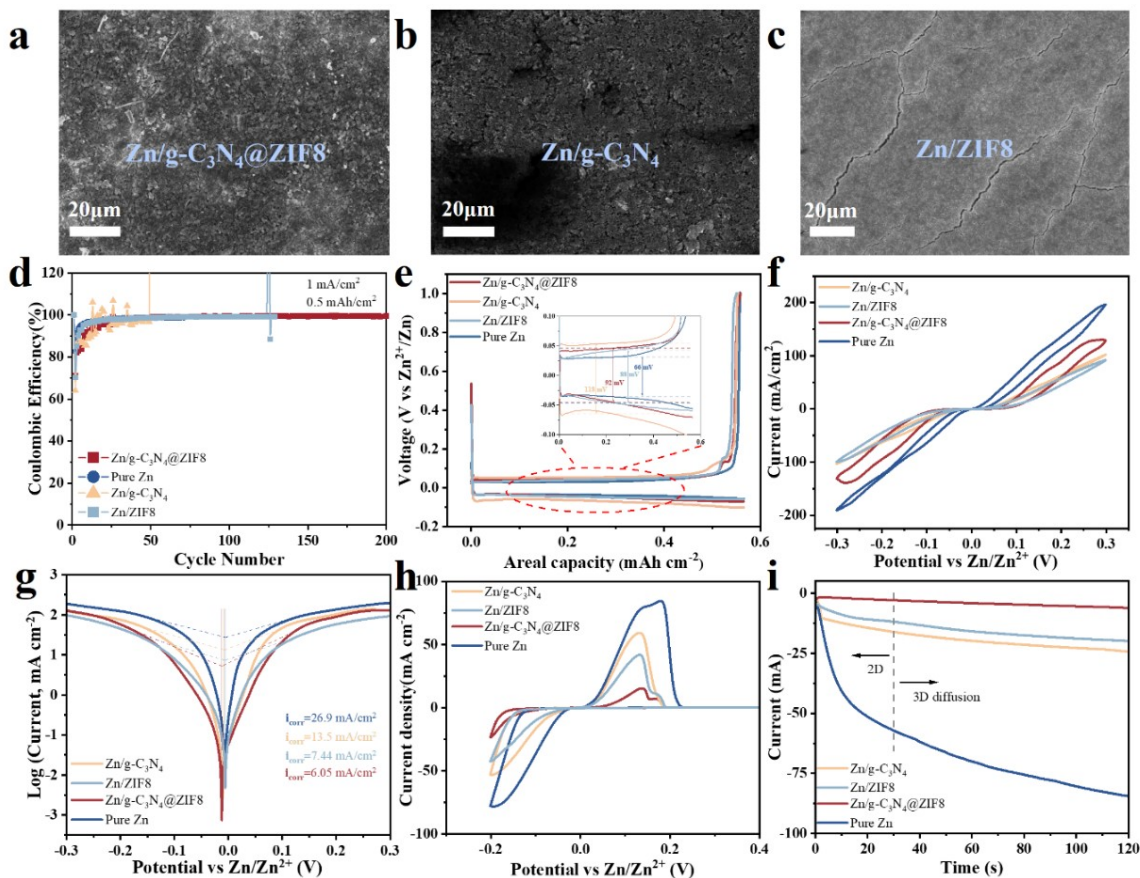
Figure 27. Top-view SEM images after coating (a) g-C₃N₄@ZIF8, (b) g-C₃N₄ and (c) ZIF8 on Zn foil; (d) CE test of coated and bare Zn anodes; (e) Comparison of charge-discharge curves at 50 th cycle from CE test; (f) Cyclic voltammetry(CV) results of the assembled symmetric cells; (g) Linear polarization curves of coated and bare Zn; (h) CV test for Zn nucleation on coated Cu foil and bare foil; (i) Chronoamperograms of coated Zn and bare Zn.
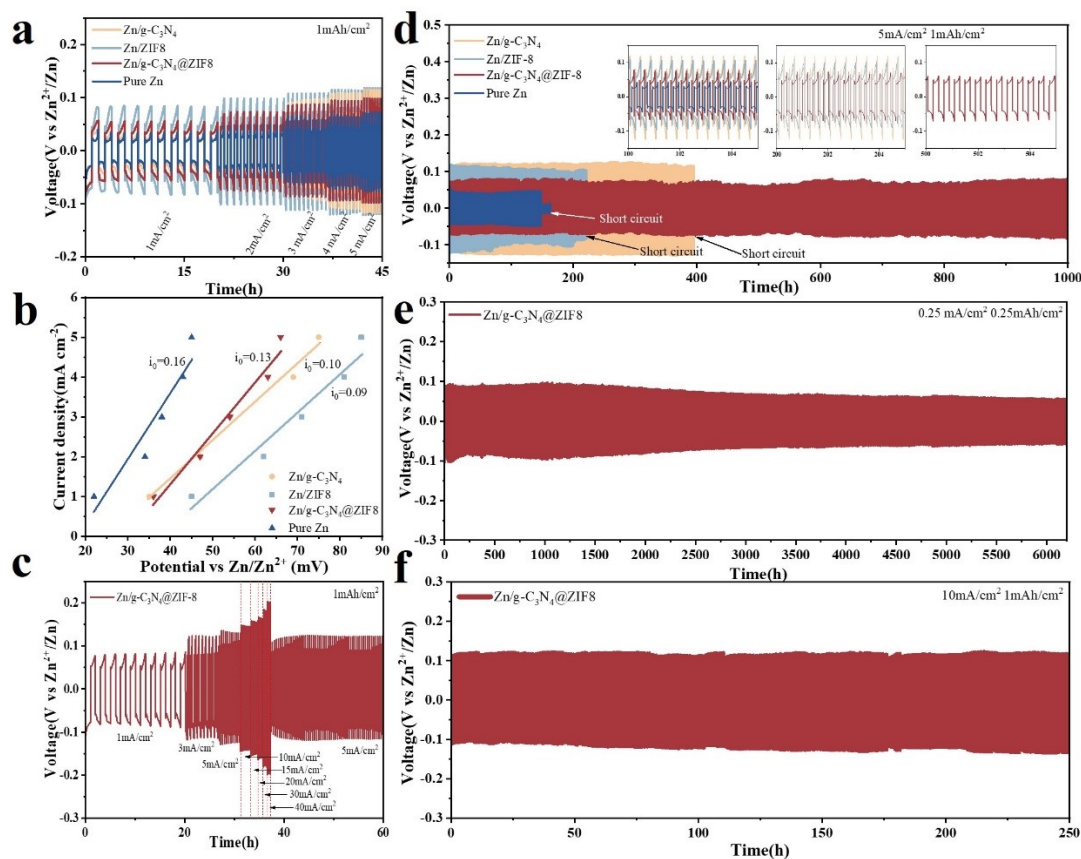
Figure 28. (a) Rate performance of the symmetric cells at 1 ,2 ,3 ,4 and 5 mA cm^{-2}; (b) Plots of the potential against current density of the symmetric cells; (c) Rate performance of symmetric cell tested from 1 to 3 ,5 ,10 ,15 ,20 ,30 , and 40 mA cm^{-2}; (d) Long-term cycling of symmetrical cell using bare and coated Zn at 5 mA cm^{-2}/1 mAh cm^{-2}. Long-term cycling of symmetrical cell using Zn/g-C3N4@ZIF8 at (e) 0.25 mA cm^{-2}/0.25 mAh cm^{-2} and (f) 10 mA cm^{-2}/1 mAh cm^{-2}.

In order to compare the stability and rate capability of the protected Zn anodes, galvanostatic cycling of symmetric cells is tested under various areal capacities and different current densities. **Figure 28. a** and **Figure 28. c** show the rate performances of symmetric cells. As shown in **Figure 28. a**, the Zn/g-C$_3$N$_4$@ZIF8 anode exhibits the lowest overpotential among all coated anodes under 1 to 5 mA cm^{-2}, while the pure Zn anode shows a lower overpotential than all coated anodes. This

58

can be explained by the low dielectric constant of both g-C$_3$N$_4$ and ZIF8, which means that the Zn ions require more energy to traverse the protective layer[90, 93]. Additionally, **Figure 28. b** shows the exchange current density of samples calculated by the function [101] of

$$i \approx i_0 \frac{2F\eta}{RT} \qquad (5)$$

where i is running current density, i_o is the exchange current density, F and R, are Faradic and gas constant, respectively. T is temperature, and η is total overpotential. As a higher exchange current density indicates a higher deposition kinetic[101], the Zn/g-C$_3$N$_4$@ZIF8 anode exhibits a similar current density of 1.67 mA cm^{-2} to the pure Zn (2.05 mA cm^{-2}) which is a proof of faster kinetic compared to Zn/ZIF8 (1.15 mA cm^{-2}) and Zn/g-C$_3$N$_4$ (1.28 mA cm^{-2}).

Furthermore, the Zn/g-C$_3$N$_4$@ZIF8 symmetric cell was further measured at various current densities from 1 to 3, 5, 10, 15, 20, 30, and 40 mA cm^{-2} (**Figure 28. c**). Impressively, the cell maintains a stable voltage hysteresis even at an ultrahigh rate of 40 mA cm^{-2}. In addition to its exceptional high-rate capability, its stability is excellent as well. As shown in **Figure 28. d**, the Zn/g-C$_3$N$_4$@ZIF8 anode can cycle for 1000 hours with a low overpotential of 50 mV under 5mA cm^{-2} and 1mAh cm^{-2}, while the bare Zn anode, Zn/g-C$_3$N$_4$ and Zn/ZIF8 only have lifespans of 150 h, 400 h, and 220 h with the overpotentials of 30 mV, 80 mV and 75 mV, respectively (insets of **Figure 28. c**). The g-C$_3$N$_4$@ZIF8 protective layer has demonstrated its effectiveness in prolonging the lifespan of Zn anodes and suppressing the dendrite growth and side reactions. This is attributed to the presence of zincophilic ZIF8 nanoparticles, which provide additional ionic paths within the g-C$_3$N$_4$ nanosheets, thereby regulating the flow of Zn ions and preventing the blocking of ionic diffusion that occurs in pure g-C$_3$N$_4$ samples. The symmetrical cells with Zn/g-C$_3$N$_4$@ZIF8 anodes were also tested under other current densities and capacities. As depicted in **Figure 28. e**, the Zn/g-C$_3$N$_4$@ZIF8 keeps stable running for over 6200h, with a low and steady voltage hysteresis of

around 110 mV under 0.25 mA cm^{-2}/0.25 mAh cm^{-2}. The charge-discharge curves shown in **Fig. S3** further verified the exceptional stability and reversibility of Zn/g-C$_3$N$_4$@ZIF8 due to the nearly overlapped curves under different cycles. Further increasing the current density to 10 mA cm^{-2} (**Figure 28. f**), the Zn/g-C$_3$N$_4$@ZIF8 anode can achieve long cycles of over 250 h. These results demonstrate that high-rate and long-lived Zn metal anodes can be realized by coating g-C$_3$N$_4$@ZIF8, which is comparable to many reported Zn anodes (**Table S1**)[85, 103-112]. The electrochemical impedance spectroscopy (EIS) was also performed to study the interfacial transport resistance of the coating layer in the assembled symmetric cells.
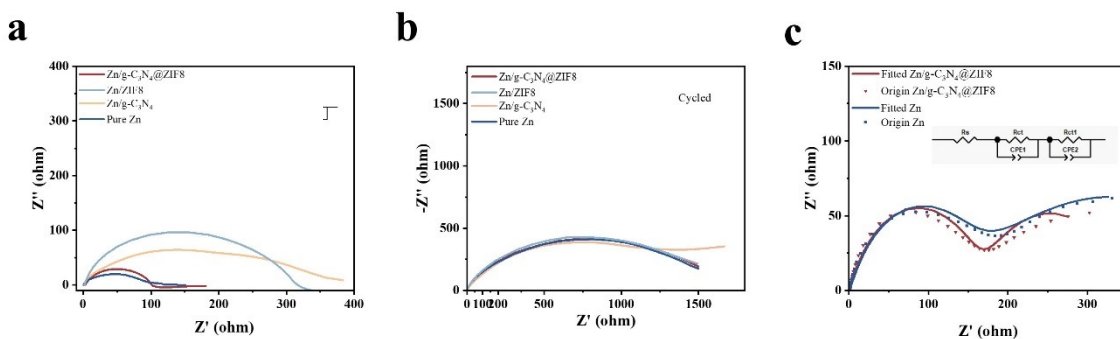
Figure 29. Nyquist plots of symmetric cells (a) before (b) after cycles and (c) fitted curves of uncycled cells.

As shown in **Figure 29. a**, it is clear that the Zn/g-C$_3$N$_4$@ZIF8 electrode shows a smaller interface impedance compared to that of the Zn/g-C$_3$N$_4$ and Zn/ZIF8. Such result should be mainly attributed to the excellent ionic-conductivity and zincophilic properties of the g-C$_3$N$_4$@ZIF8 coating layer, which allow the efficient transport kinetics at the anode/electrolyte interface. After ten times cycling, the interface impedances of all electrodes (**Figure 29. b**) keep the same trend and get increase due to the formation of an insoluble Zn(OH)$_2$ layer, the formation of dendrites, and the degradation of the electrolyte, which can be verified by the cross-sectional SEM images after cycles. **Figure 29. c** is the fitted curves of uncycled cells, the inset is the equivalent circuit,

Rs is the ohmic internal resistance, CPE is the constant phase elements which is used in a model in place of a capacitor to compensate for non-homogeneity in the system. For example, a rough or porous surface can cause a double-layer capacitance to appear as a constant phase element, Rct is the cathode charge transfer resistance. From the EIS spectra, the Zn/g-C$_3$N$_4$@ZIF8 electrode and pure zinc anode show similar performance in high frequency zone, and Zn/g-C$_3$N$_4$@ZIF8 maintained a lower impedance compared to the pure zinc anode, it also can be justified in the **Table S2.** In the high frequency domain, the number of Rct, CPE1-T and CPE1-P showed similar amounts, it indicates similar performance. However, under low frequency domain, the number of Rct, CPE2-T and CPE2-P of pure zinc anode increase dramatically, which means that the Zn/g-C$_3$N$_4$@ZIF8 electrode has lower capacitance and lower cathode transfer resistance. These parameters validate the Zn/g-C$_3$N$_4$@ZIF8 has better low frequency performance, whereas the AZIBs are mostly running under DC (Direct current) condition.
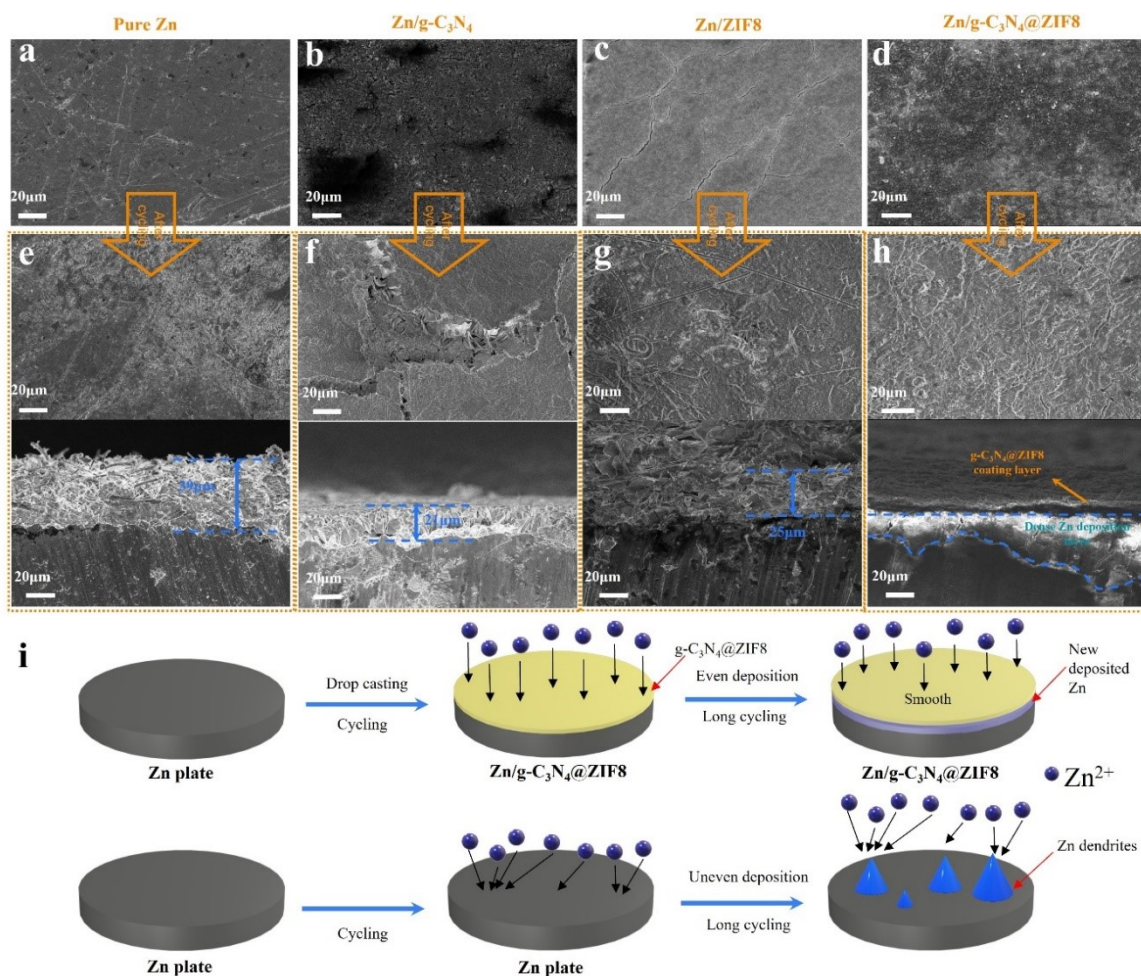
Figure 30. (a-d) Top-view SEM images of uncycled anodes; (e-h) Top-view and cross-sectional SEM images of cycled anodes (150 h of pure Zn, 400 h of Zn/g-C$_3$N$_4$, 250 h of Zn/ZIF8 and 1000 h Zn/g-C$_3$N$_4$@ZIF8; (i) The scheme of Zn/g-C$_3$N$_4$@ZIF8 and pure Zn plate after long cycling.

In order to further testify the superiority of g-C$_3$N$_4$@ZIF8 on the anode protection, SEM tests are performed to compare the pristine and cycled morphology of Zn/g-C$_3$N$_4$@ZIF8, Zn/g-C$_3$N$_4$, Zn/ZIF8 and pure Zn. It is commonly noted that the longer cycling, the surface morphology of anodes would have a more severe deformation. **Figure 30. d** and **h** display the surface change of Zn/g-C$_3$N$_4$@ZIF8 from a flat and relatively smooth surface to a less smooth but no dendritic surface even after cycling for 1000 hours. In comparison, pure Zn, Zn/g-C$_3$N$_4$ and Zn/ZIF8 anodes

show severe cracks and obvious hexagonal nanoflakes of Zn dendrites on the surface (**Figure 30. e-g**). Additionally, the deposited Zn layer can be further clearly distinguished from the cross-sectional SEM images. As shown in **Figure 30. h**, the cycled Zn/g-C$_3$N$_4$@ZIF8 anode illustrates a dense and uniform deposited Zn layer under the g-C$_3$N$_4$@ZIF8 coating layer with no dendrites getting through the protective layer. For cycled pure Zn anode (**Figure 30. e**), many dendrites emerged to form a 39 μm-thick loose layer. As to Zn/g-C$_3$N$_4$ and Zn/ZIF8, the protecting layer no longer exists anymore (**Figure 30. f-g**) due to the Zn dendrites growing through the layer and forming a thick and mixed depositing layer (21 μm of Zn/g-C$_3$N$_4$ and 25 μm of Zn/ZIF8), which may be caused by the self-stacking property of g-C$_3$N$_4$ [111] and cracks of uncycled ZIF8 layer which can be clearly observed in **Figure 30. c**. The improved performance of g-C$_3$N$_4$@ZIF8 in resisting deformation is mainly attributed to the self-suspending structure of the g-C$_3$N$_4$@ZIF8 particles. This structure helps regulate the flux of Zn ions, thereby slowing down the formation of tips on the surface of the anode. This ultimately slows down the dendrite growth speed that is typically caused by the "tip effect". As illustrated in **Figure 30. i**, the use of a g-C$_3$N$_4$@ZIF8 protective layer on Zn anodes enables more uniform and dense deposition. In contrast, uneven deposition of Zn occurs on bare Zn, leading to the formation of Zn dendrites. To investigate the mechanism of the g-C$_3$N$_4$@ZIF8 protective layer on the Zn deposition process, we employed density functional theory (DFT) to calculate the absorption process of Zn atoms on g-C$_3$N$_4$ and ZIF8. As shown in **Fig. S4-S5**, the adsorption energy of Zn atoms on ZIF8 and g-C$_3$N$_4$ is 0.61 eV and 0.29 eV, respectively. As the adsorption energy of g-C$_3$N$_4$ is lower than that of bare Zn (0.34 eV) [116] and the stacking of g-C$_3$N$_4$, the diffusion pattern of Zn^{2+} tends to random diffusion. ZIF8 has higher adsorption energy than pure Zn, but the ZIF8 cannot form an even coating layer, as discussed above. Thus single ZIF8 as a coating layer couldn't regulate Zn flux efficiently. Whereas the g-C$_3$N$_4$@ZIF8 can handle the task of Zn ion regulation due to the supporting of ZIF8 in the interstitial layer of g-C$_3$N$_4$. The presence of ZIF8 in the interstitial layer of g-C$_3$N$_4$ enhances the adsorption capacity for Zn^{2+} ions in g-C$_3$N$_4$@ZIF8, resulting in a more efficient adsorption process

compared to the 2D diffusion of Zn^{2+} on Zn surfaces. Furthermore, this leads to a strong 3D diffusion of Zn^{2+} within the g-C_3N_4@ZIF8 composite. As a result, it promotes the desolvation and uniform distribution of Zn^{2+} flux at the electrode-electrolyte interface, ensuring dendrite-free Zn deposition.
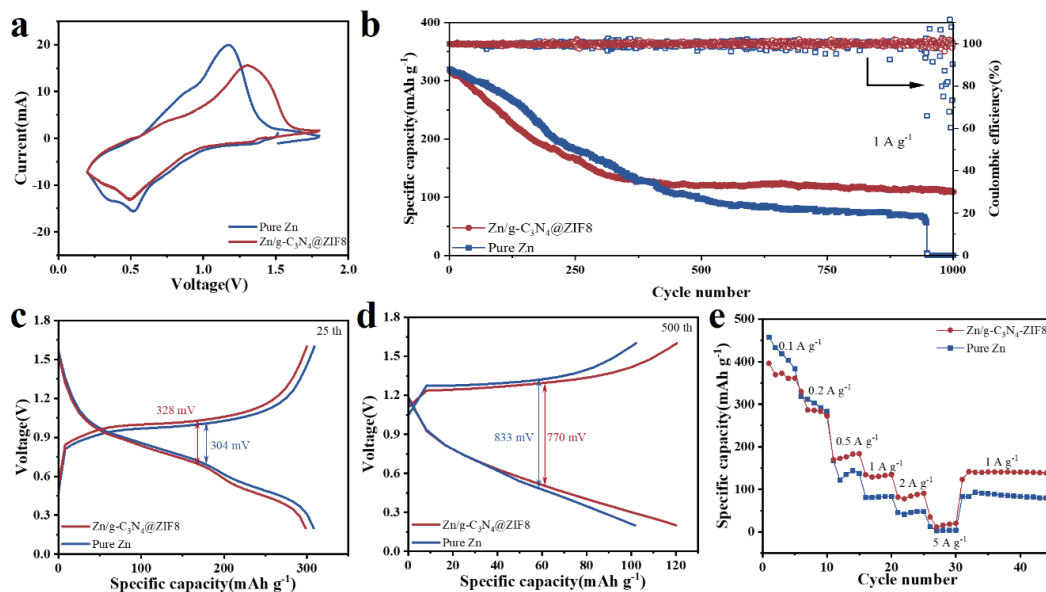
Figure 31. (a) CV profiles of Zn||V_2O_5 full cells with bare Zn and Zn/g-C_3N_4@ZIF8 anodes for 1st cycle; (b) Galvanostatic cycling performance of full cells at 1 A g^{-1}; Galvanostatic charge/discharge profiles at (c) 25th cycle and (d) 500th cycle; (e) Rate performance tested under different current densities.

To further evaluate the practical application of the Zn/g-C_3N_4@ZIF8, full cells were assembled with V_2O_5 nanopaper as cathodes[43]. The preparation of the V_2O_5 nanopaper is described in the experimental section. The cyclic voltammetry (CV) profiles at a scan rate of 1 mV s^{-1} are displayed in **Figure 31. a**. Lower response current and larger potential separation in this voltage window range can be seen when employing the Zn/g-C_3N_4@ZIF8 as the anode. Also, a similar performance can be seen in the galvanostatic cycling test. As shown in **Figure 31. b**, before 400 cycles, the full

64

cell with Zn/g-C$_3$N$_4$@ZIF8 illustrates lower capacity than the full cell with pure Zn anode. This phenomenon can also be verified by the galvanostatic charge/discharge (GCD) profiles of both samples at 1 A g^{-1}, shown in **Figure 31. c-d**. The polarization potential of Zn/g-C$_3$N$_4$@ZIF8||V$_2$O$_5$ cell is 328 mV and voltage profiles maintain well after 25 cycles, which is higher than 304 mV of bare Zn||V$_2$O$_5$ cell. On the contrary, the full cell with Zn/g-C$_3$N$_4$@ZIF8 possesses a much lower polarization potential of 770 mV than that of bare Zn anode (833 mV) after 500 cycles. The difference can be explained by the descriptions in **Figure 30**. In the early cycle, the surface passivation after coating an insulating g-C$_3$N$_4$@ZIF8 layer on conductive Zn is the main reason. Then as the cycle proceeds, pure Zn anode can generate much more Zn dendrites and enhance the polarization, while the Zn/g-C$_3$N$_4$@ZIF8 anode can prohibit the dendrites formation and result in a weak polarization. Also, the full cell with Zn/g-C$_3$N$_4$@ZIF8 coated anode can achieve a specific capacity of 300 mAh g^{-1} and maintain at 120 mAh g^{-1} even after 1,000 cycles, as the pure Zn anode can only last for 943 cycles with a fast decay and short-circuit after then. Hence, the g-C$_3$N$_4$@ZIF8 protective layer can significantly extend the lifespan of batteries. Furthermore, the rate performance of both full cells using bare Zn and Zn/g-C$_3$N$_4$@ZIF8 is shown in **Figure 31. e**. The cell with a Zn/g-C$_3$N$_4$@ZIF8 anode exhibits higher capacities than the cell with a bare Zn anode at current densities of 0.1, 0.2, 0.5,1.0, 2.0, 5.0 and 1.0 A g^{-1}, respectively. The superior performance demonstrates the improvement in the Zn reversibility achieved by the g-C$_3$N$_4$@ZIF8 coating on the anode.

4.4. Conclusion

In summary, a stable and inert particle g-C$_3$N$_4$@ZIF8 is assigned as a protecting interlayer between the anode surface and electrolyte for preventing side reactions and corrosion on the zinc, which are prime culprits of dendrites and short circuits. The g-C$_3$N$_4$@ZIF8 can constrain the zinc ion flux irregularities by restricting the path from the electrolyte to the anode surface, which will aid zinc

deposition stability and consistency. Consequently, the g-C_3N_4@ZIF8 covered zinc anode lasted for 1,000 hours at 5mA cm^{-2} and 6200 hours at 0.25mA cm^{-2} in symmetric cells, which are remarkably longer lifespan compared to pure Zn anode. In the CE test, the cell can achieve 99.4% efficiency. Regarding the full cell test, Zn/g-C_3N_4@ZIF8||V_2O_5 lasts longer than Zn||V_2O_5 and can conserve a higher capacity. This work provides a more simplistic and efficient strategy for building a dendrite-free and long-lasting protecting layer between the electrolyte and the anode in aqueous zinc ion batteries.

Chapter 5 Conclusion and Prospectives

5.1 Conclusion

AZIBs are being considered as a highly promising option for grid-scale energy storage shortly. This is due to their favorable characteristics, such as low cost, high safety levels, and environmental friendliness. Surface modification of the zinc metal anode is a promising strategy to address the problems of dendrite formation and side reactions that severely hinder the stability and efficiency of aqueous Zn-ion batteries (AZIBs). This approach involves altering the surface properties of the anode to regulate the reaction between the anode and electrolyte and mitigate dendrite formation and corrosion. The unique characteristics of surface materials, such as physical, electrical, and chemical properties, play important roles in zinc anode protection by physically suppressing dendrite, accelerating zinc ions diffusion rate and inducing even deposition of Zn ion flux.

In Chapter 1, the demand for high-performance AZIBS and short-terms of present zinc anode was described and discussed.

Chapter 2 proposed a thorough review of recently published coating materials. In this review, coating materials were categorized into two kinds, inorganic and organic. In this review, every sample's unique feature, mechanism, symmetric and full cell performances were discussed and summarized, which can provide a relatively detailed and logical vision of surface modification. Hopefully, this review will help design and fabricate high performance AZIBs.

Chapter 3 described the methodologies and techniques used in my project.

In Chapter 4, a series of experiments was established to test a synergistic artificial interlayer material, g-C_3N_4@ZIF8. From the results of experiments, the g-C_3N_4@ZIF8 can restrict the zinc flux irregularities and aid zinc deposition stability and consistency. Consequently, the g-C_3N_4@ZIF8 covered zinc anode lasted for 1000 h at 5mA cm^{-2} and 6200 h at 0.25mA cm^{-2} in

symmetric cells, which are remarkably longer lifespan compared to pure Zn anode. In the CE test, the cell can achieve 99.4% efficiency. Regarding the full cell test, Zn/g-C$_3$N$_4$@ZIF8$\|$V$_2$O$_5$ lasts longer than Zn$\|$V$_2$O$_5$ and can conserve a higher capacity. This study proposes a simpler and more effective approach to creating a durable protective layer between the anode and electrolyte in aqueous zinc-ion batteries, which can prevent dendrite formation and improve the battery's longevity. These results provide further support for the important role that artificial interlayers play in flexible and environmentally adaptive AZIBs, as discussed in Chapter 1.

5.2 Prospectives

There are still challenges with the zinc anode protection. (1) It is necessary to gain a deeper understanding of the mechanisms behind the zinc deposition and stripping. The zinc dendrite growth model research is not as developed as lithium metal, which can hinder further research on AZIB. Further investigation is required by in-situ techniques and simulation methods to better understand the dendrite's growth process. (2) The correlation between the electrochemical performance associated with the deposition product and a sound database of different coating materials is preferred, like the dendrite structure and current density relationship, which can better aid the researchers in designing new materials and monitoring the performance without using SEM. It can be time-saving and efficient. (3) Each strategy aimed at protecting the zinc anode has limitations and unique drawbacks. Furthermore, some of these strategies operate via similar mechanisms. Therefore, a comprehensive and well-designed combination of multiple strategies is expected to achieve more effective and long-lasting protection. Additionally, some of these strategies may be applied to protect other metal electrodes used in various energy storage systems.

References

[1] Huang J, Guo Z, Ma Y, et al. Recent progress of rechargeable batteries using mild aqueous electrolytes[J]. Small Methods, 2019, 3(1): 1800272.

[2] Xie J, Lu Y C. A retrospective on lithium-ion batteries[J]. Nature communications, 2020, 11(1): 2499.

[3] Wang F, Borodin O, Gao T, et al. Highly reversible zinc metal anode for aqueous batteries[J]. Nature materials, 2018, 17(6): 543-549.

[4] Wang, et al. Highly reversible zinc metal anode for aqueous batteries. Nat Mater. (2018).

[5] Yang D, Tan H, Rui X, et al. Electrode materials for rechargeable zinc-ion and zinc-air batteries: current status and future perspectives[J]. Electrochemical Energy Reviews, 2019, 2: 395-427.

[6] Jia X, Liu C, Neale Z G, et al. Active materials for aqueous zinc ion batteries: synthesis, crystal structure, morphology, and electrochemistry[J]. Chemical Reviews, 2020, 120(15): 7795-7866.

[7] Zhang R, Chen X R, Chen X, et al. Lithiophilic sites in doped graphene guide uniform lithium nucleation for dendrite-free lithium metal anodes[J]. Angewandte Chemie, 2017, 129(27): 7872-7876.

[8] Li X, Chu Z, Jiang H, et al. Redistributing Li-ion flux and homogenizing Li-metal growth by N-doped hierarchically porous membranes for dendrite-free Lithium metal batteries[J]. Energy Storage Materials, 2021, 37: 233-242.

[9] Liu B, Wang S, Wang Z, et al. Novel 3D nanoporous Zn–Cu alloy as long-life anode toward high-voltage double electrolyte aqueous zinc-ion batteries[J]. Small, 2020, 16(22): 2001323.

[10] Li B, Zhang X, Wang T, et al. Interfacial engineering strategy for high-performance Zn metal anodes[J]. Nano-Micro Letters, 2022, 14: 1-31.

[11] Zhao Z, Li P, Zhang Z, et al. Dendrite-free zinc anode enabled by Buffer-like additive via strong cationic specific absorption[J]. Chemical Engineering Journal, 2023, 454: 140435.

[12] Zeng X, Zhao J, Wan Z, et al. Controllably electrodepositing ZIF-8 protective layer for highly reversible zinc anode with ultralong lifespan[J]. The Journal of Physical Chemistry Letters, 2021, 12(37): 9055-9059.

[13] Yuan L, Hao J, Kao C C, et al. Regulation methods for the Zn/electrolyte interphase and the effectiveness

evaluation in aqueous Zn-ion batteries[J]. Energy & Environmental Science, 2021, 14(11): 5669-5689.

[14] Kang, Litao, et al. "Nanoporous $CaCO_3$ coatings enabled uniform Zn stripping/plating for long‐life zinc rechargeable aqueous batteries." Advanced Energy Materials 8.25 (2018): 1801090.

[15] Deng W, Zhang N, Wang X. Hybrid interlayer enables dendrite-free and deposition-modulated zinc anodes[J]. Chemical Engineering Journal, 2022, 432: 134378.

[16] Liu P, Zhang Z, Hao R, et al. Ultra-highly stable zinc metal anode via 3D-printed $g\text{-}C_3N_4$ modulating interface for long life energy storage systems[J]. Chemical Engineering Journal, 2021, 403: 126425.

[17] Li B, Xue J, Lv X, et al. A facile coating strategy for high stability aqueous zinc ion batteries: Porous rutile nano-TiO2 coating on zinc anode[J]. Surface and Coatings Technology, 2021, 421: 127367.

[18] Hong L, Wu X, Wang L Y, et al. Highly reversible zinc anode enabled by a cation-exchange coating with Zn-ion selective channels[J]. ACS nano, 2022, 16(4): 6906-6915.

[19] Zhou J, Xie M, Wu F, et al. Ultrathin surface coating of nitrogen-doped graphene enables stable zinc anodes for aqueous zinc-ion batteries[J]. Advanced Materials, 2021, 33(33): 2101649.

[20] Deng C, Xie X, Han J, et al. A sieve-functional and uniform-porous kaolin layer toward stable zinc metal anode[J]. Advanced Functional Materials, 2020, 30(21): 2000599.

[21] Liu B, Zhang J G, Xu W. Advancing lithium metal batteries[J]. Joule, 2018, 2(5): 833-845.

[22] Han C, Li W, Liu H K, et al. Principals and strategies for constructing a highly reversible zinc metal anode in aqueous batteries[J]. Nano Energy, 2020, 74: 104880.

[23] Zheng, Jingxu, et al. "Spontaneous and field-induced crystallographic reorientation of metal electrodeposits at battery anodes." Science advances 6.25 (2020): eabb1122.

[24] Du W, Ang E H, Yang Y, et al. Challenges in the material and structural design of zinc anode towards high-performance aqueous zinc-ion batteries[J]. Energy & Environmental Science, 2020, 13(10): 3330-3360.

[25] Han, Chao, et al. "Principals and strategies for constructing a highly reversible zinc metal anode in aqueous batteries." Nano Energy 74 (2020): 104880.

[26] Shin J, Lee J, Park Y, et al. Aqueous zinc ion batteries: focus on zinc metal anodes[J]. Chemical science, 2020, 11(8): 2028-2044.

[27] Zhang, Qi, et al. "Interfacial design of dendrite‐free zinc anodes for aqueous zinc‐ion batteries." Angewandte Chemie International Edition 59.32 (2020): 13180-13191.

[28] Li, Canpeng, et al. "Issues and future perspective on zinc metal anode for rechargeable aqueous zinc‐ion batteries." Energy & Environmental Materials 3.2 (2020): 146-159..

[29] Fu, Jing, et al. "Electrically rechargeable zinc–air batteries: progress, challenges, and perspectives." Advanced materials 29.7 (2017): 1604685.

[30] Lu, Wenjing, et al. "Inhibition of zinc dendrite growth in zinc‐based batteries." ChemSusChem 11.23 (2018): 3996-4006.

[31] Wang, Anran, et al. "Modifying the Zn anode with carbon black coating and nanofibrillated cellulose binder: A strategy to realize dendrite-free Zn-MnO$_2$ batteries." Journal of Colloid and Interface Science 577 (2020): 256-264.

[32] Liu, Penggao, et al. "Ultra-highly stable zinc metal anode via 3D-printed g-C$_3$N$_4$ modulating interface for long life energy storage systems." Chemical Engineering Journal 403 (2021): 126425.

[33] Li, Ming, et al. "A novel dendrite‐free Mn^{2+}/Zn^{2+} hybrid battery with 2.3 V voltage window and 11000‐cycle lifespan." Advanced Energy Materials 9.29 (2019): 1901469.

[34] Liang, Yongchang, et al. "Functionalized carbon nanofiber interlayer towards dendrite-free, Zn-ion batteries." Chemical Engineering Journal 425 (2021): 131862.

[35] Zhou, Zhubo, et al. "Graphene oxide-modified zinc anode for rechargeable aqueous batteries." Chemical Engineering Science 194 (2019): 142-147.

[36] Xia, Aolin, et al. "Graphene oxide spontaneous reduction and self-assembly on the zinc metal surface enabling a dendrite-free anode for long-life zinc rechargeable aqueous batteries." Applied Surface Science 481 (2019): 852-859.

[37] Zhou, Jiahui, et al. "Ultrathin surface coating of nitrogen‐doped graphene enables stable zinc anodes for aqueous zinc‐Ion batteries." Advanced Materials 33.33 (2021): 2101649.

[38] Li, Zhiwei, et al. "Pencil drawing stable interface for reversible and durable aqueous zinc-ion batteries." Advanced Functional Materials 31.4 (2021): 2006495.

[39] Zhao, Yang, et al. "Carbon paper interlayers: a universal and effective approach for highly stable Li metal

anodes." *Nano Energy* 43 (2018): 368-375.

[40] Zhao, Kangning, et al. "Ultrathin surface coating enables stabilized zinc metal anode." *Advanced Materials Interfaces* 5.16 (2018): 1800848.

[41] Kang L, Cui M, Jiang F, et al. Nanoporous CaCO3 coatings enabled uniform Zn stripping/plating for long-life zinc rechargeable aqueous batteries[J]. *Advanced Energy Materials*, 2018, 8(25): 1801090.

[42] Deng, Canbin, et al. "A sieve‑functional and uniform‑porous kaolin layer toward stable zinc metal anode." *Advanced Functional Materials* 30.21 (2020): 2000599.

[43] Yan H, Li S, Nan Y, et al. Ultrafast zinc–ion–conductor interface toward high-rate and stable zinc metal batteries[J]. *Advanced Energy Materials*, 2021, 11(18): 2100186.

[44] Han, Jin, et al. "A thin and uniform fluoride-based artificial interphase for the zinc metal anode enabling reversible Zn/MnO$_2$ batteries." *ACS Energy Letters* 6.9 (2021): 3063-3071.

[45] Cai, Zhao, et al. "Chemically resistant Cu–Zn/Zn composite anode for long cycling aqueous batteries." *Energy Storage Materials* 27 (2020): 205-211.

[46] Liu, Cheng, et al. "Liquid alloy interlayer for aqueous zinc-ion battery." *ACS Energy Letters* 6.2 (2021): 675-683.

[47] Lu, Qiongqiong, et al. "Uniform Zn deposition achieved by Ag coating for improved aqueous zinc-ion batteries." *ACS Applied Materials & Interfaces* 13.14 (2021): 16869-16875.

[48] Han, Daliang, et al. "A corrosion‑resistant and dendrite‑free zinc metal anode in aqueous systems." *Small* 16.29 (2020): 2001736.

[49] Guo, W., et al. "Multifunctional tin layer enabled long-life and stable anode for aqueous zinc-ion batteries." *Materials Today Energy* 20 (2021): 100675.

[50] Zeng, Xiaohui, et al. "Recent progress and perspectives on aqueous Zn-based rechargeable batteries with mild aqueous electrolytes." *Energy Storage Materials* 20 (2019): 410-437.

[51] Hoang, Tuan KA, Kyung Eun Kate Sun, and P. J. R. A. Chen. "Corrosion chemistry and protection of zinc & zinc alloys by polymer-containing materials for potential use in rechargeable aqueous batteries." *RSC Advances* 5.52 (2015): 41677-41691.

[52] Hieu, Luong Trung, et al. "Zn anode with flexible β-PVDF coating for aqueous Zn-ion batteries with long cycle life." Chemical Engineering Journal 411 (2021): 128584.

[53] Zhang, Qi, et al. "Interfacial design of dendrite‐free zinc anodes for aqueous zinc‐ion batteries." Angewandte Chemie International Edition 59.32 (2020): 13180-13191.

[54] Zhao, Zhiming, et al. "Long-life and deeply rechargeable aqueous Zn anodes enabled by a multifunctional brightener-inspired interphase." Energy & Environmental Science 12.6 (2019): 1938-1949.

[55] Xu, Airong, et al. "Composites from biodegradable and biocompatible methylcellulose, poly (d, l‐lactide‐co‐glycolide) and poly (1, 4‐butylene succinate) with enhanced properties." Journal of Applied Polymer Science 138.18 (2021): 50320.

[56] Zeng, Xiaomin, et al. "Controllably Electrodepositing ZIF-8 Protective Layer for Highly Reversible Zinc Anode with Ultralong Lifespan." The Journal of Physical Chemistry Letters 12.37 (2021): 9055-9059.

[57] Liu, Xiaoqing, et al. "Zeolitic imidazolate frameworks as Zn^{2+} modulation layers to enable dendrite‐free Zn anodes." Advanced Science 7.21 (2020): 2002173.

[58] Yuksel, Recep, et al. "Metal‐organic framework integrated anodes for aqueous zinc‐ion batteries." Advanced Energy Materials 10.16 (2020): 1904215.

[59] Yang, Huijun, et al. "Constructing a super‐saturated electrolyte front surface for stable rechargeable aqueous zinc batteries." Angewandte Chemie 132.24 (2020): 9463-9467.

[60] Chen, Peng, et al. "An artificial polyacrylonitrile coating layer confining zinc dendrite growth for highly reversible aqueous zinc‐based batteries." Advanced Science 8.11 (2021): 2100309.

[61] Li, Bin, et al. "A facile coating strategy for high stability aqueous zinc ion batteries: Porous rutile nano-TiO_2 coating on zinc anode." Surface and Coatings Technology 421 (2021): 127367.

[62] He, Huibing, et al. "Highly stable Zn metal anodes enabled by atomic layer deposited Al_2O_3 coating for aqueous zinc-ion batteries." Journal of materials chemistry A 8.16 (2020): 7836-7846.

[63] Zhang, Binghan, et al. "Effect of kaolin content on the performances of kaolin-hybridized soybean meal-based adhesives for wood composites." Composites Part B: Engineering 173 (2019): 106919.

[64] Khamsanga, Sonti, et al. "Polypyrrole/reduced graphene oxide composites coated zinc anode with dendrite

suppression feature for boosting performances of zinc ion battery." Scientific Reports 12.1 (2022): 8689.

[65] Liu, Penggao, et al. "Ultra-highly stable zinc metal anode via 3D-printed g-C$_3$N$_4$ modulating interface for long life energy storage systems." Chemical Engineering Journal 403 (2021): 126425.

[66] Cao, Penghui, et al. "Fast‑charging and ultrahigh‑capacity zinc metal anode for high‑performance aqueous zinc‑ion batteries." Advanced Functional Materials 31.20 (2021): 2100398.

[67] Hao, Junnan, et al. "Designing dendrite‑free zinc anodes for advanced aqueous zinc batteries." Advanced Functional Materials 30.30 (2020): 2001263.

[68] Zhang, Feng, et al. "Polypyrrole-controlled plating/stripping for advanced zinc metal anodes." Materials Today Energy 17 (2020): 100443.

[69] Cao, Ziyi, et al. "Eliminating Zn dendrites by commercial cyanoacrylate adhesive for zinc ion battery." Energy Storage Materials 36 (2021): 132-138.

[70] Jia X, Liu C, Neale Z G, et al. Active materials for aqueous zinc ion batteries: synthesis, crystal structure, morphology, and electrochemistry [J]. Chemical Reviews, 2020, 120(15): 7795-866.

[71] Zhang R, Chen X R, Chen X, et al. Lithiophilic sites in doped graphene guide uniform lithium nucleation for dendrite‑free lithium metal anodes [J]. Angewandte Chemie, 2017, 129(27): 7872-6.

[72] Li X, Chu Z, Jiang H, et al. Redistributing Li-ion flux and homogenizing Li-metal growth by N-doped hierarchically porous membranes for dendrite-free Lithium metal batteries [J]. Energy Storage Materials, 2021, 37: 233-42.

[73] Liu B, Wang S, Wang Z, et al. Novel 3D nanoporous Zn–Cu alloy as long‑life anode toward high‑voltage double electrolyte aqueous zinc‑ion batteries [J]. Small, 2020, 16(22): 2001323.

[74] Li B, Zhang X, Wang T, et al. Interfacial engineering strategy for high-performance Zn metal anodes [J]. Nano-Micro Letters volume 2022, 14: 1-31.

[75] Zhao Z, Li P, Zhang Z, et al. Dendrite-free zinc anode enabled by Buffer-like additive via strong cationic specific absorption [J]. Chemical Engineering Journal, 2023, 454: 140435.

[76] Zeng X, Zhao J, Wan Z, et al. Controllably Electrodepositing ZIF-8 Protective Layer for Highly Reversible Zinc Anode with Ultralong Lifespan [J]. The Journal of Physical Chemistry Letters, 2021, 12(37): 9055-9.

[77] Yuan L, Hao J, Kao C-C, et al. Regulation methods for the Zn/electrolyte interphase and the effectiveness evaluation in aqueous Zn-ion batteries [J]. Energy & Environmental Science, 2021, 14(11): 5669-89.

[78] Han C, Li W, Liu H K, et al. Principals and strategies for constructing a highly reversible zinc metal anode in aqueous batteries [J]. Nano Energy, 2020, 74: 104880.

[79] Liu P, Zhang Z, Hao R, et al. Ultra-highly stable zinc metal anode via 3D-printed g-C_3N_4 modulating interface for long life energy storage systems [J]. Chemical Engineering Journal, 2021, 403: 126425.

[80] Zhou J, Xie M, Wu F, et al. Ultrathin Surface Coating of Nitrogen-Doped Graphene Enables Stable Zinc Anodes for Aqueous Zinc-Ion Batteries [J]. Advanced Materials, 2021, 33(33): 2101649.

[81] Deng C, Xie X, Han J, et al. A sieve-functional and uniform-porous kaolin layer toward stable zinc metal anode [J]. Advanced Functional Materials, 2020, 30(21): 2000599.

[82] He H, Tong H, Song X, et al. Highly stable Zn metal anodes enabled by atomic layer deposited Al_2O_3 coating for aqueous zinc-ion batteries [J]. Journal of materials chemistry A, 2020, 8(16): 7836-46.

[83] Deng W, Zhang N, Wang X J C E J. Hybrid interlayer enables dendrite-free and deposition-modulated zinc anodes [J]. Chemical Engineering Journal, 2022, 432: 134378.

[84] Li B, Xue J, Lv X, et al. A facile coating strategy for high stability aqueous zinc ion batteries: Porous rutile nano-TiO2 coating on zinc anode [J]. Surface and Coatings Technology, 2021, 421: 127367.

[85] Zhou M, Guo S, Fang G, et al. Suppressing by-product via stratified adsorption effect to assist highly reversible zinc anode in aqueous electrolyte [J]. Journal of Energy Chemistry, 2021, 55: 549-56.

[86] Miao Z, Du M, Li H, et al. Constructing nano-channeled tin layer on metal zinc for high-performance zinc-ion batteries anode [J]. EcoMat, 2021, 3(4): e12125.

[87] Chen P, Yuan X, Xia Y, et al. An artificial polyacrylonitrile coating layer confining zinc dendrite growth for highly reversible aqueous zinc-based batteries [J]. Advanced Science, 2021, 8(11): 2100309.

[88] Hong L, Wu X, Wang L-Y, et al. Highly reversible zinc anode enabled by a cation-exchange coating with Zn-ion selective channels [J]. ACS Nano, 2022, 16(4): 6906-15.

[89] Xu Z, Jin S, Zhang N, et al. Efficient Zn metal anode enabled by O, N-codoped carbon microflowers [J]. Nano Letters, 2022, 22(3): 1350-7.

[90] Huang J, Guo Z, Ma Y, et al. Recent progress of rechargeable batteries using mild aqueous electrolytes [J]. Small Methods, 2019, 3(1): 1800272.

[91] Xie J, Lu Y-C J N C. A retrospective on lithium-ion batteries [J]. Nature communications, 2020, 11(1): 2499.

[92] Zhou L, Yang F, Zeng S, et al. Zincophilic Cu Sites Induce Dendrite-Free Zn Anodes for Robust Alkaline/Neutral Aqueous Batteries [J]. Advanced Functional Materials, 2022, 32(15): 2110829.

[93] Yu H, Zeng Y, Li N W, et al. Confining Sn nanoparticles in interconnected N-doped hollow carbon spheres as hierarchical zincophilic fibers for dendrite-free Zn metal anodes [J]. Science Advances, 2022, 8(10): eabm5766.

[94] Xie F, Li H, Wang X, et al. Mechanism for zincophilic sites on zinc-metal anode hosts in aqueous batteries [J]. Advanced Energy Materials, 2021, 11(9): 2003419.

[95] Wang C, Gao Y, Sun L, et al. Anti-catalytic and zincophilic layers integrated zinc anode towards efficient aqueous batteries for ultra-long cycling stability [J]. Nano Research 2022, 15(9): 8076-82.

[96] Yang Q, Guo Y, Yan B, et al. Hydrogen-substituted graphdiyne ion tunnels directing concentration redistribution for commercial-grade dendrite-free zinc anodes [J]. Advanced Materials, 2020, 32(25): 2001755.

[97] Wang X, Yang K, Ma C, et al. N-Rich carbon as Zn^{2+} modulation layers for dendrite-free, highly reversible zinc anodes [J]. Chemical Engineering Journal, 2023, 452: 139257.

[98] Wen J, Xie J, Chen X, et al. A review on g-C_3N_4-based photocatalysts [J]. Applied surface science, 2017, 391: 72-123.

[99] Yang Y, Chen T, Yu B, et al. Manipulating Zn-ion flux by two-dimensional porous g-C_3N_4 nanosheets for dendrite-free zinc metal anode [J]. Chemical Engineering Journal, 2022, 433: 134077.

[100] Hayat A, Al-Sehemi A G, El-Nasser K S, et al. Graphitic carbon nitride (g–C_3N_4)–based semiconductor as a beneficial candidate in photocatalysis diversity [J]. International Journal of Hydrogen Energy, 2022, 47(8): 5142-91.

[101] Wang Y, Guo T, Yin J, et al. Controlled deposition of zinc-metal anodes via selectively polarized ferroelectric polymers [J]. Advanced Materials, 2022, 34(4): 2106937.

[102] Wei C, Tan L, Zhang Y, et al. Metal-organic frameworks and their derivatives in stable Zn metal anodes for aqueous Zn-ion batteries [J]. ChemPhysMater, 2022, 1(4): 252-63.

[103] Eslava S, Zhang L, Esconjauregui S, et al. Metal-organic framework ZIF-8 films as low-κ dielectrics in microelectronics [J]. Chemistry of Materials, 2013, 25(1): 27-33.

[104] Yuan X, Qu S, Huang X, et al. Design of core-shelled g-$C_3N_4@$ ZIF-8 photocatalyst with enhanced tetracycline adsorption for boosting photocatalytic degradation [J]. Chemical Engineering Journal, 2021, 416: 129148.

[105] Kohn W, Sham L J. Self-Consistent Equations Including Exchange and Correlation Effects [J]. Physical Review, 1965, 140(4A): A1133-A8.

[106] Liu Y, Li Y, Huang X, et al. Copper Hexacyanoferrate Solid-State Electrolyte Protection Layer on Zn Metal Anode for High-Performance Aqueous Zinc-Ion Batteries [J]. Small, 2022, 18(38): 2203061.

[107] Abdallah M J C S. Ethoxylated fatty alcohols as corrosion inhibitors for dissolution of zinc in hydrochloric acid [J]. Corrosion science, 2003, 45(12): 2705-16.

[108] Chai S, Zhang Y, Wang Y, et al. Biodegradable composite polymer as advanced gel electrolyte for quasi-solid-state lithium-metal battery [J]. eScience, 2022, 2(5): 494-508.

[109] Hu Y, Fu C, Chai S, et al. Construction of zinc metal-Tin sulfide polarized interface for stable Zn metal batteries [J]. Advanced Powder Materials, 2023, 2(2): 100093.

[110] Yang Y, Liu C, Lv Z, et al. Synergistic manipulation of Zn^{2+} ion flux and desolvation effect enabled by anodic growth of a 3D ZnF_2 matrix for long-lifespan and dendrite-free Zn metal anodes [J]. Advanced Materials, 2021, 33(11): 2007388.

[111] Huang C, Zhao X, Liu S, et al. Stabilizing zinc anodes by regulating the electrical double layer with saccharin anions [J]. Advanced Materials, 2021, 33(38): 2100445.

[112] Dong J, Zhang Y, Hussain M I, et al. g-C_3N_4: Properties, pore modifications, and photocatalytic applications [J]. Nanomaterials, 2022, 12(1): 121.

[113] Gan H, Wu J, Li R, et al. Ultra-stable and deeply rechargeable zinc metal anode enabled by a multifunctional protective layer [J]. Energy Storage Mater, 2022, 47: 602-10.

[114] Li Y, Huang Z, Kalambate P K, et al. V_2O_5 nanopaper as a cathode material with high capacity and long cycle life for rechargeable aqueous zinc-ion battery [J]. Nano Energy, 2019, 60: 752-9.

[115] Tian, R., Park, SH., King, P.J. et al. Quantifying the factors limiting rate performance in battery electrodes. Nat

Commun 10, 1933 (2019).

[116] H. Gan, J. Wu, R. Li, B. Huang, H. Liu, Ultra-stable and deeply rechargeable zinc metal anode enabled by a multifunctional protective layer, Energy Storage Mater. 47 (2022) 602-610.

[117] Deng W, Xu Z, Wang X. High-donor electrolyte additive enabling stable aqueous zinc-ion batteries[J]. Energy Storage Materials, 2022, 52: 52-60.

[118] Yang Y, Liu C, Lv Z, et al. Synergistic manipulation of Zn^{2+} ion flux and desolvation effect enabled by anodic growth of a 3D ZnF_2 matrix for long‐lifespan and dendrite‐free Zn metal anodes[J]. Advanced Materials, 2021, 33(11): 2007388.

[119] Zhou M, Guo S, Fang G, et al. Suppressing by-product via stratified adsorption effect to assist highly reversible zinc anode in aqueous electrolyte[J]. Journal of Energy Chemistry, 2021, 55: 549-556.

[120] Chen P, Yuan X, Xia Y, et al. An artificial polyacrylonitrile coating layer confining zinc dendrite growth for highly reversible aqueous zinc‐based batteries[J]. Advanced Science, 2021, 8(11): 2100309.

[121] Hong L, Wu X, Wang L Y, et al. Highly reversible zinc anode enabled by a cation-exchange coating with Zn-ion selective channels[J]. ACS nano, 2022, 16(4): 6906-6915.

[122] Gracia, J., and P. Kroll. "Corrugated layered heptazine-based carbon nitride: the lowest energy modifications of C_3N_4 ground state." Journal of Materials Chemistry 19.19 (2009): 3013-3019.

[123] Venna S R, Jasinski J B, Carreon M A. Structural evolution of zeolitic imidazolate framework-8[J]. Journal of the American Chemical Society, 2010, 132(51): 18030-18033.

[124] Zhao Z, Sun Y, Luo Q, et al. Mass-controlled direct synthesis of graphene-like carbon nitride nanosheets with exceptional high visible light activity. Less is better[J]. Scientific reports, 2015, 5(1): 14643.

[125] Liu S, Chen F, Li S, et al. Enhanced photocatalytic conversion of greenhouse gas CO_2 into solar fuels over g-C_3N_4 nanotubes with decorated transparent ZIF-8 nanoclusters[J]. Applied Catalysis B: Environmental, 2017, 211: 1-10.

[126] Yuan X, Qu S, Huang X, et al. Design of core-shelled g-C_3N_4@ ZIF-8 photocatalyst with enhanced tetracycline adsorption for boosting photocatalytic degradation[J]. Chemical Engineering Journal, 2021, 416: 129148.
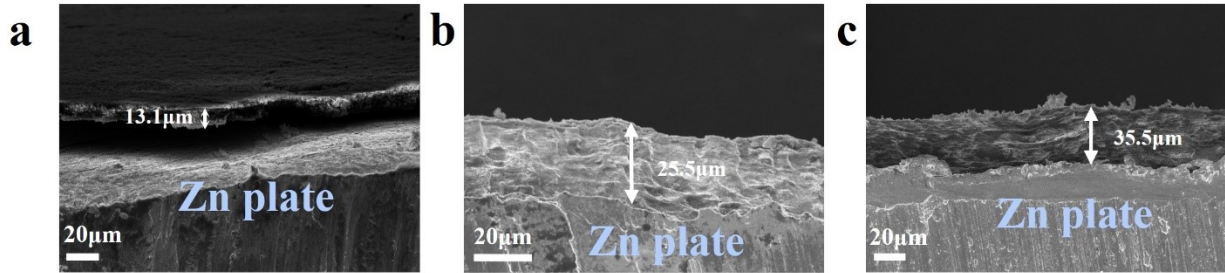
78

Appendix

Fig. S1. Cross-sectional SEM images after coating (a) g-C$_3$N$_4$@ZIF8, (b) g-C$_3$N$_4$ and (c) ZIF8 on Zn foil;
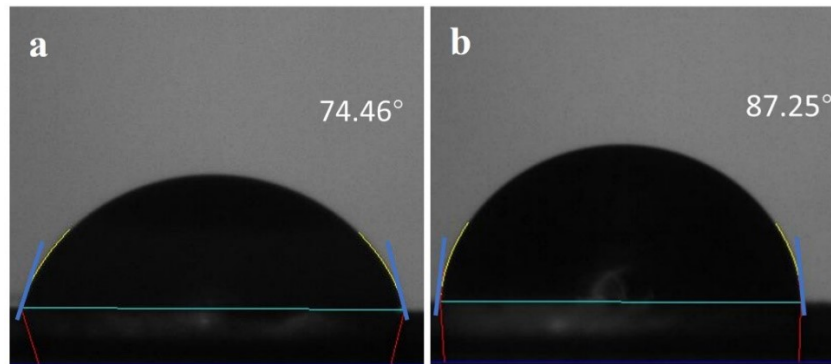

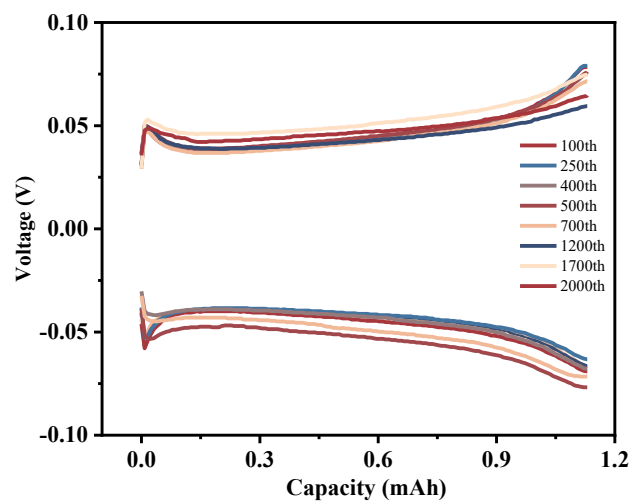Fig. S2 contact angle measurement of (a) g-C$_3$N$_4$@ZIF8 (b)pure zinc.

Fig. S3. Charging and discharging voltage profile of Zn/C$_3$N$_4$@ZIF-8 symmetric cell under 0.25 mA cm^{-2}/0.25 mAh cm^{-2}.
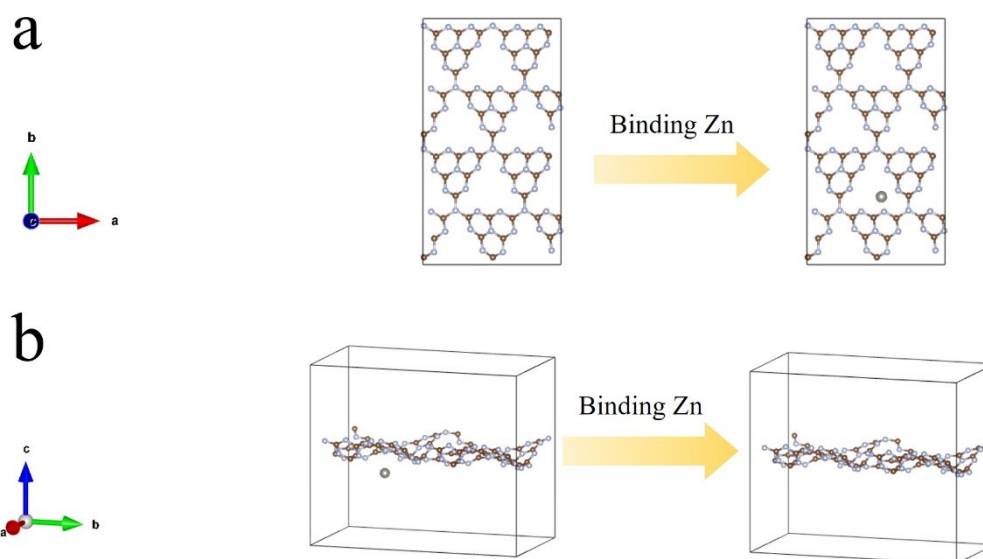

Fig. S4. The 3D optimized configurations of a Zn atom absorbed on a single layer of g-C$_3$N$_4$ in (a) top and (b) 3D views.
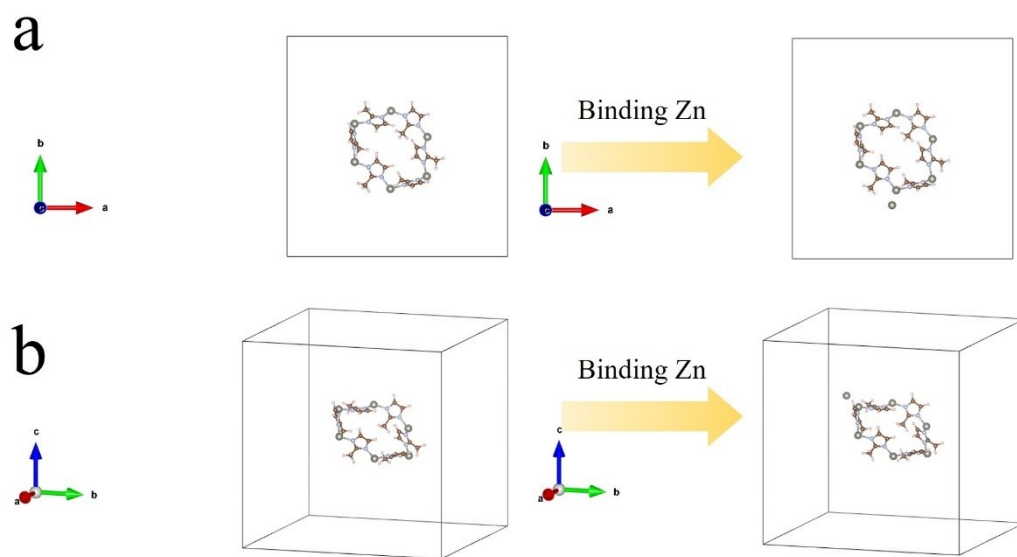
Fig. S5. The 3D optimized configurations of a Zn atom absorbed on the unit cell of ZIF-8 in (a) top and (b) 3D views.

Table S1 A survey of modified Zn anodes and corresponding electrochemical properties in Zn‖Zn symmetric cells.

	Symmetric cells			
Sample	Current density (mA cm^{-2}), capacity	Voltage hysteresis	Cycle life	Reference
Zn/C$_3$N$_4$@ZIF-8	0.25, 0.25	110mV	3500h	This work
	5, 1	115mV	1000h	This work
	10, 1	150mV	250h	This work
Zn/C$_3$N$_4$	2,2	~80mV	500h	[32]
	10,5	~200mV	120h	
Zn/ZnO/C	0.25,0.25	56mV	2000h	[15]
	2,1	~80mV	500h	
	5,1	~150mV	700h	
	10,2.5	~200mV	240h	
Zn/TiO$_2$	1,1	40.9mV	150h	[40]
Zn/Sc$_2$O$_3$	1,1	71mV	200h	[48]
	0.5,0.5	~55mV	300h	
	2,2	~40 mV	250h	
Zn/Polyacrylonitrile	1,1	75mV	1145h	[49]
Zn/PFSA	1,0.5	~80mV	1500h	[50]
	1,1	~90mV	800h	
Zn/NGO	1,1	34mV	1200h	[37]
	5,5	96mV	300h	
Zn/Al$_2$O$_3$	1,1	36.5mV	500h	[62]
Zn/Kaolin	4.4,1.1	~140mV	800h	[42]
Zn/Sn	1,1	28mV	800h	[49]

Table S2 A table of fitted EIS results.

Circuit Parts	Samples	
	Zn	Zn/C$_3$N$_4$@ZIF-8
Rs (Ω)	0.589	0.746
Rct (Ω)	140	160
CPE1-T	$2.02*10^{-2}$	$2.56*10^{-3}$
CPE1-P	0.745	0.72
Rct1 (Ω)	386.6	180
CPE2-T	$8.28*10^{-2}$	$2.13*10^{-2}$
CPE2-P	0.396	0.6

Rs is the internal ohmic resistance of the cell; Rct is the cathode charge transfer resistance; CPE-T is the amplitude of the Constant Phase Element; CPE-P is the phase angle ratio of the Constant Phase Element.